# Non-canonical glutamine transamination sustains efferocytosis by coupling redox buffering to oxidative phosphorylation

Johanna Merlin, Stoyan Ivanov, Adélie Dumont, Alexey Sergushichev, Julie Gall, Marion Stunault, Marion Ayrault, Nathalie Vaillant, Alexia Castiglione, Amanda Swain, et al.

Published in final edited form as:
*Nat Metab*. 2021 October 01; 3(10): 1313–1326. doi:10.1038/s42255-021-00471-y.

# Non-canonical glutamine transamination sustains efferocytosis by coupling redox buffering to oxidative phosphorylation

**Johanna Merlin**[#1], **Stoyan Ivanov**[#1], **Adélie Dumont**[#1], **Alexey Sergushichev**[2], **Julie Gall**[1], **Marion Stunault**[1], **Marion Ayrault**[1], **Nathalie Vaillant**[1], **Alexia Castiglione**[1], **Amanda Swain**[3], **Francois Orange**[4], **Alexandre Gallerand**[1], **Thierry Berton**[5], **Jean-Charles Martin**[5], **Stefania Carobbio**[6,7], **Justine Masson**[8], **Inna Gaisler-Salomon**[9], **Pierre Maechler**[6], **Stephen Rayport**[9], **Judith C. Sluimer**[10], **Erik A. L. Biessen**[10,11], **Rodolphe R. Guinamard**[1], **Emmanuel L. Gautier**[12], **Edward B. Thorp**[13], **Maxim N. Artyomov**[3], **Laurent Yvan-Charvet**[1]

[1]Institut National de la Santé et de la Recherche Médicale (Inserm) U1065, Université Côte d'Azur, Centre Méditerranéen de Médecine Moléculaire (C3M), Centre national de la recherche scientifique (CNRS) (R.G.), Atip-Avenir, Fédération Hospitalo-Universitaire (FHU) Oncoage, 06204 Nice, France

[2]Computer Technologies Department, ITMO University, Saint Petersburg, Russia

[3]Department of Pathology and Immunology, Washington University School of Medicine, St. Louis, MO, USA

[4]Université Côte d'Azur, Centre Commun de Microscopie Appliquée (CCMA), 06108 Nice, France

[5]Centre de Recherche Cardiovasculaire et Nutritionnelle (C2VN), INSERM, Institut National de la Recherche Agricole (INRA), BioMet, Aix-Marseille University, Marseille, France

[6]Department of Cell Physiology and Metabolism: University of Geneva Medical Centre, Geneva, Switzerland

[7]Wellcome Trust Sanger Institute, Wellcome Trust Genome Campus, Hinxton, UK; Metabolic Research Laboratories, Addenbrooke's Treatment Centre, Institute of Metabolic Science, Addenbrooke's Hospital, University of Cambridge, Cambridge, UK

[8]Inserm UMR-S1270, Institut du Fer à Moulin, Sorbonne Université, Paris F-75005, France)



Correspondence to: Laurent Yvan-Charvet.

Address correspondence to LYC: yvancharvet@unice.fr.

***Author Contributions***.

L.Y.-C. conceived the project, designed the experiments, and wrote the manuscript. J.M., S.I., and A.D. performed most of the molecular, histological, and *in vivo* experiments. A.S., J.G., M.S., M.A., N.V., A.C., A.S., and A.G. helped with the experimental design and assisted with the data analysis. F.O., T.B., and J.C.M. provided access to platform facilities and assisted with the data acquisition and analysis. S.C., J.M., I.G.S., P.M., and S.R. provided transgenic mice and intellectual discussion. J.C.S., and E.A.L.B aided in the design and analysis of human studies. R.R., and E.L.G., E.B.T., M.N.A. provided scientific advice and helped with the experimental design. L.Y.-C. also designed and supervised the study and obtained funding. All of the authors read, edited, and approved the manuscript.

**Conflict of interest.**

The authors declare no conflict of interest.


Europe PMC Funders Author Manuscripts

[9]Department of Psychiatry, Columbia University, USA; Department of Molecular Therapeutics, NYS Psychiatric Institute, USA and SPC-IBBR, University of Haifa, Israel

[10]Department of Pathology, Cardiovascular Research Institute Maastricht, Maastricht University Medical Center, Maastricht, the Netherlands

[11]Institute for Molecular Cardiovascular Research, RWTH Klinikum Aachen, Germany

[12]Sorbonne Université, INSERM, UMR_S 1166 ICAN, F-75013 Paris, France

[13]Department of Pathology, Northwestern University, Feinberg School of Medicine, Chicago, Illinois 60611, USA

[#] These authors contributed equally to this work.

## Summary

Macrophages rely on tightly integrated metabolic rewiring to clear dying neighboring cells by efferocytosis during homeostasis and disease. Here, we reveal that glutaminase (GLS) 1-mediated glutaminolysis is critical to promote apoptotic cell clearance by macrophages during homeostasis in mice. In addition, impaired macrophage glutaminolysis exacerbates atherosclerosis, a condition during which efficient apoptotic cell debris clearance is critical to limit disease progression. Gls1 expression strongly correlates with atherosclerotic plaque necrosis in patients with cardiovascular diseases. High-throughput transcriptional and metabolic profiling reveals that macrophage efferocytic capacity relies on a non-canonical transaminase pathway, independent from the traditional requirement of glutamate dehydrogenase (GLUD1) to fuel α-ketoglutarate-dependent immunometabolism. This pathway is necessary to meet the unique requirements of efferocytosis for cellular detoxification and high energy cytoskeletal rearrangements. Thus, we uncover a role for non-canonical glutamine metabolism for efficient clearance of dying cells and maintenance of tissue homeostasis during health and disease in mouse and humans

### Keywords

Macrophage; Glutaminolysis; Efferocytosis; Interleukin-4 and Atherosclerosis

## Introduction

Clearance of apoptotic cells (ACs) by macrophages (i.e, efferocytosis) prevents the leakage of dying cellular contents to maintain tissue integrity in normal physiology[1,2]. Impaired efferocytosis in disease can have multiple causes, but defects in the internalization of multiple ACs, a process termed ‘continual efferocytosis’, has emerged as a culprit of many chronic inflammatory diseases such as atherosclerosis[3,4]. Resolution and repair processes also require the cytokine interleukin-4 (IL-4)[5], and an efficient cellular metabolic reprogramming to sustain continual efferocytosis[6]. However, the understanding of metabolism during efferocytosis on a molecular level is still poorly understood and fundamentally and clinically relevant.

Glutamine metabolism is considered as a ‘fuel for the immune system’ and is routinely used as a component for clinical supplementation in trauma patients. Glutamine is

initially hydrolyzed into glutamate by the glutaminase GLS1 in a metabolic process called glutaminolysis[7,8], which is the most upregulated pathway in reparative-type macrophages induced by IL-4 dependent alternative activation[9]. Yet, whether glutaminolysis supports the functional metabolic reprogramming of efferocytosis beyond glucose and fatty acid metabolism remains unknown[10,11].

Here, we tested the hypothesis that glutaminolysis plays a critical role in macrophage efferocytic capacity. Mice lacking macrophage *Gls1* exhibited defective efferocytosis *in vivo* and *in vitro* under reparative conditions or upon successive rounds of exposure to dying cells. The clinical and pathologic relevance of glutaminolysis in this process was exemplified with the inverse association with the accumulation of necrotic core in human and murine atherosclerotic lesions. Mechanistically, glutaminolysis channeled glutamate into the malate-aspartate shuttle through an aspartate aminotransferase (GOT)-dependent transamination process to meet the demand for cellular detoxification and cytoskeletal rearrangements and achieve efficient efferocytosis.

## Results

### Macrophage glutaminolysis orchestrates optimal efferocytosis

To investigate metabolic roles of macrophage glutaminolysis during clearance functions, mice bearing a conditional allele for glutaminase 1 (*Gls1* $^{fl/fl}$) in macrophages were generated by crossing to Lysozyme M-Cre transgenic mice (LysM-Cre). LysM-Cre x *Gls1* $^{fl/fl}$ peritoneal cavity macrophages (Mac$^{\Delta Gls1}$ PCMs) efficiently deleted GLS1 and presented with a 2-fold decrease in cellular glutamate levels as compared to controls (Fig. 1a). Glutaminolysis can control the balance between cellular life and death *in vitro* through mTORC1 pathway or ferroptosis, respectively[12,13]. Although *Gls1* was expressed to various levels in PCMs, bone marrow (BM) monocytes/macrophages, red pulp macrophages (RPMs), Kupffer cells and microglia (Extended Data Fig. 1a), their numbers were unaltered in Mac$^{\Delta Gls1}$ mice (Extended Data Fig. 1b). Consistently, proliferation and apoptosis were similar in Mac$^{\Delta Gls1}$ PCMs compared to control cells (Extended Data Fig. 1c). Levels of phospho-S6 and Myc protein, mTORC1 downstream targets, were also unchanged in these cells (Extended Data Fig. 1d) along with absence of transcriptional regulation of rapamycin (mTOR), hypoxia or ferroptosis targets (Extended Data Fig. 1e). These data strongly suggested that glutaminolysis is not required for macrophage maintenance or development at steady state. Consistent with the strong enrichment in glutaminolytic processes in IL-4 treated reparative macrophages[9], we observed an impaired induction of canonical alternatively activated genes (*Clec10a, Tgm2, Arg1, Stab1, Sepp1*) (Extended Data Fig. 1f) and cell surface expression of CD206 and CD301 (Extended Data Fig. 1g) in Mac$^{\Delta Gls1}$ PCMs. Additionally, challenging PCMs with either IL-4, apoptotic cells (ACs) or IL-4 and ACs together revealed that GLS1-dependent glutaminolysis was required for efficient efferocytosis in reparative macrophages. We measured an approximately 20% phagocytic index reduction in IL-4 stimulated Mac$^{\Delta Gls1}$ TIMD4$^{+}$ PCM subsets after 45 min exposure to apoptotic thymocytes (Fig. 1b). A similar trend was observed in the less efferocytic TIMD4$^{-}$ PCM subset (Fig. 1b). This occurred independently of transcriptional changes in key efferocytic receptors such as *MertK*, *Timd4* or *Gas6* or immunoregulatory cytokines

such as *Tgfβ* or *Il-10* in reparative Mac$^{\Delta Gls1}$ PCMs (Extended Data Fig. 1h). Consistently, IL-10 secretion levels were unaltered in these cells (Extended Data Fig. 1h). Nevertheless, these responses were specific of AC clearance as similar percentage of heat-killed *E.coli* phagocytosis was observed between control and Mac$^{\Delta Gls1}$ PCMs (Extended Data Fig. 1i). Defects in efferocytic responses were also confirmed using IL-4 primed reparative bone marrow-derived macrophages (BMDMs) (Fig. 1c). Importantly, overexpression of *Gls1* in BMDMs using lentiviral particles enhanced efferocytosis in un-stimulated control cells and rescued the defective efferocytosis observed in reparative Mac$^{\Delta Gls1}$ macrophages (Fig. 1d). To test the impact of glutaminolysis on efferocytosis during heightened metabolic challenge, we subjected *Gls1*-deficient macrophages to successive rounds of AC clearance, which mimics tissue states of high cell turnover[6]. We performed a validated two-stage efferocytosis experiment in which BMDMs were first incubated for 45min with unlabeled ACs and, after AC removal and a one-hour interval, incubated with a second round of labelled ACs[3]. Under these conditions, the percentage of resolving macrophages that had internalized the second round of ACs was significantly decreased in *Gls1*-deficient macrophages relative to controls (Fig. 1e). To test the *in vivo* significance, we intravenously injected fluorescently labeled ACs into controls and Mac$^{\Delta Gls1}$ mice. *Gls1* deficiency reduced the ability of CD11b$^{lo}$F4/80$^{high}$ Kupffer cells (KCs) in the liver and red pulp macrophages (RPMs) in the spleen and to some extent CD11b$^{high}$F4/80$^{high}$ monocyte-derived macrophages (MoMacs) to internalize labeled ACs one hour after injection (Fig. 1f). These findings provide *in vivo* genetic evidence of the pivotal role of GLS1-dependent glutaminolysis during macrophage phagocytic clearance.

## Glutaminolysis regulates efferocytosis in atherosclerosis

We next tested GLS1 requirements in a mouse model of atherosclerosis, in which defective lesional dead cell clearance translates into unstable necrotic core within plaques[1,14]. Taking advantage of publicly available gene expression datasets of western diet (WD) fed wild-type (WT) and *Apoe*-deficient mice[15], we observed a downregulation of *Gls1* expression in atheromatous plaques. This was part of a dysregulated amino acid catabolism module making up a densely connected core with a more global metabolic transcriptome signature (Extended Data Fig. 2a). Lower *Gls1* expression correlated with an imbalance in markers of inflammatory and reparative macrophages (Heatmap, Extended Data Fig. 2a). To monitor glutaminolysis activity in atherosclerotic plaque, we next assessed radiolabeled [$^{14}$C] glutamine uptake and hydrolysis in aortas extracted from WT and *Apoe*$^{-/-}$ mice fed on WD for 6 weeks. Biomolecular imaging revealed higher glutamine incorporation into plaque areas enriched in macrophages (Extended Data Fig. 2b). Nevertheless, quantification of [$^{14}$C] glutamine conversion into glutamate, after separation by thin-layer chromatography, confirmed lower glutaminase-dependent metabolism in atherosclerotic aorta (Extended Data Fig. 2c). Next, mice with macrophage-specific deletion of *Gls1* (Mac$^{\Delta Gls1}$ mice) were crossed onto an atherosclerotic *Apoe*-deficient background. After WD feeding (12 weeks), there was an approximately 1.7-fold increase in atherosclerosis plaque area in the aortic sinus compared to co-housed control littermates (Fig. 2a). Oil red O staining in descending aortas confirmed higher plaque burden in *Apoe*$^{-/-}$ Mac$^{\Delta Gls1}$ mice (Fig. 2b) despite similar plasma lipid levels (Extended Data Fig. 2d). Increased plaque area was also visualized in an independent cohort of *Apoe*$^{-/-}$ Mac$^{\Delta Gls1}$ mice using non-invasive ultrasound imaging

(Fig. 2c). These effects were specific to macrophage glutaminolysis since hematopoietic *Gls1*-deficiency (i.e, generation of Mx1-Cre x *Gls1* $^{fl/fl}$ mice onto the atherosclerotic *Apoe*$^{-/-}$ background, referred as *Apoe*$^{-/-}$ HSC$^{\Delta Gls1}$ mice) recapitulated similar accelerated atherosclerosis relative to control animals (Extended Data Fig. 2e). Further characterization of atherosclerotic lesions in *Apoe*$^{-/-}$ Mac$^{\Delta Gls1}$ mice revealed complex plaques containing macrophages (Extended Data Fig. 2f). We did not observe significant change in Ki67-positive proliferative cells in *Apoe*$^{-/-}$ Mac$^{\Delta Gls1}$ mice (Extended Data Fig. 2f). In contrast, necrotic cores were typified by a greater proportion of TUNEL-positive free ACs and a reduced proportion of macrophage associated ACs, a hallmark of defective efferocytosis (Fig. 2d). By injecting fluorescent dye-labeled apoptotic lymphocytes intraperitoneally, we confirmed the reduced ability of peritoneal macrophages from *Apoe*$^{-/-}$ Mac$^{\Delta Gls1}$ mice to efficiently perform efferocytosis (Extended Data Fig. 2g). To examine clinical significance, we investigated whether *Gls1* expression correlated with human atherosclerotic plaque complexity. We found a reduced *Gls1* expression in unstable *vs*. stable human carotid artery plaque (Fig. 2e). Moreover, we uncovered a positive correlation between *Gls1* expression and the M2-specific marker Arg1$^{+}$ (Fig. 2e). By contrast, *Gls1* levels inversely correlated with plaque size, intraplaque hemorrhage (IPH) and necrotic core composition (Fig. 2e), key markers of atherosclerosis severity. Taken together, our findings demonstrate that GLS1 contributes to AC engulfment in the pathological process of human and murine atherosclerosis.

## Glutaminolysis supports efferocytosis by fueling OXPHOS

We next found that intracellular *Gls1* mRNA expression was similarly upregulated by IL-4 stimulation or AC ingestion in a validated gene expression dataset (Extended Data Fig. 3a)[5]. We confirmed this upregulation in a time course experiment (Extended Data Fig. 3b), paralleling a drop in cellular glutamine to glutamate ratio (Extended Data Fig. 3c). To identify how glutamine-dependent pathways are regulated in reparative macrophages, we traced $^{13}$C-labeled glutamine intracellular fate and quantified several metabolites and by-products by liquid chromatography-mass spectrometry. Labeling distribution analyses revealed similar $^{13}$C incorporation into branched-chain amino acid (BC-AA), proline, glutamate $\gamma$ semialdehyde (GSA), arginine and ornithine in reparative Mac$^{\Delta Gls1}$ BMDMs, indicative of similar BC-AA catabolism and urea cycle turnover (Fig. 3a and Supplementary Table. 1). Consistently, similar levels of these compounds (i.e, leucine, valine, ornithine, arginine, proline and putrescine) were observed in Mac$^{\Delta Gls1}$ BMDMs (Extended Data Fig. 3d and 3e) and inhibition of BB-AA transferase with gabapentin or BCATi or supplementation with ornithine had no impact on the efferocytic response of reparative Mac$^{\Delta Gls1}$ BMDMs (Extended Data Fig. 3f). By contrast, lower $^{13}$C incorporation into TCA metabolites (αketoglutarate, succinate, malate and aspartate but not citrate or aconitate) was observed in reparative Mac$^{\Delta Gls1}$ BMDMs, supporting a partially defective TCA cycling in these cells (Fig. 3a). We next provided evidence of reduced basal oxygen consumption rate (OCR) and maximal respiration after FCCP treatment in Mac$^{\Delta Gls1}$ PCMs and BMDMs in comparison to control cells (Extended Data Fig. 3g and 3h). These effects occurred independently of fluctuation in extracellular acidification rate (ECAR), a surrogate of glycolytic activity (Extended Data Fig. 3i). Additionally, reduced mitochondrial complex I (i.e, NADH-ubiquinone oxidoreductase) and complex II (i.e, succinate dehydrogenase

(SDH)) activities were observed in reparative Mac$^{\Delta Gls1}$ BMDMs (Extended Data Fig. 3j). Flux measurements also showed that resting and reparative Mac$^{\Delta Gls1}$ BMDMs fed ACs exhibited a decrease in maximal respiration response (Fig. 3b and 3c). These effects were associated with a drop in ATP production reflecting an inability to fully respond to the increase in energy demand (Fig. 3d). Basal OCR and maximal respiration response were also reduced in *Gls1*-deficient macrophages during continued clearance of ACs (Extended Data Fig. 3k). Inversely, lentiviral vector-mediated overexpression of *Gls1* enhanced OCR (Extended Data Fig. 3l) and ATP production (Extended Data Fig. 3m) in control macrophages and partially rescued defects observed in reparative Mac$^{\Delta Gls1}$ BMDMs.

## Glutaminolysis induces efficient ETC during efferocytosis

The observed altered mitochondrial metabolism in resting and reparative Mac$^{\Delta Gls1}$ BMDMs was associated with higher mitochondrial reactive oxygen species (ROS) levels (Extended Data Fig. 3n) and overexpression of *Gls1* conversely limited mitochondrial ROS production (Extended Data Fig. 3o). Mitochondrial redox status has been previously shown to metabolically program macrophage effector function[16,17]. Thus, we next addressed if it could be at the origin of the defective OCR in *Gls1*-deficient macrophages. Ectopic expression of the mitochondrial alternative oxidase (AOX) from *Ciona intestinalis* improves the ubiquinone (CoQ) oxidoreduction balance by limiting build up of electrons without pumping protons for ATP synthesis (Fig. 3e)[18,19]. Overexpression of AOX abrogated the excess mitochondrial ROS production observed in reparative Mac$^{\Delta Gls1}$ BMDMs (Fig. 3f) but did not rescue the defective OCR or ATP production in these cells (Fig. 3g and Extended Data Fig. 3p). These findings suggest that mitochondrial ROS is unlikely the cause but rather a ‘by-products’ of the defective OXPHOS in *Gls1*-deficient macrophages. Additionally, mitochondrial ROS scavenging by the superoxide dismutase mimetic (Tempol) or the mitochondria-targeted antioxidant coenzyme Q10 (MitoQ) (Fig. 3e) reduced mitochondrial ROS production to the same level between genotypes (Fig. 3h), but this was insufficient to rescue the defective OCR (Fig. 3i) and efferocytic index (Fig. 3j) of reparative Mac$^{\Delta Gls1}$ BMDMs. In contrast, direct OCR inhibition by targeting SDH with 3-Nitropropionic acid (3NPA) or complex III with antimycin A (Fig. 3i), enhanced ROS generation in the mitochondria (Fig. 3h) but reduced efferocytosis in control cells to the levels of reparative Mac$^{\Delta Gls1}$ BMDMs (Fig. 3j). Similar findings were observed during continued clearance of ACs (Extended Data Fig. 3q). Consistent with the reduced OCR of Risp knockout macrophages[11], we also confirmed the genetic requirement of complex III to efferocytosis and continued clearance of ACs (Extended Data Fig. 3r). Together, these findings reveal that glutaminolysis couples mitochondrial oxidative phosphorylation to ATP production for efficient efferocytosis.

## Topological analysis of metabolic networks

To elucidate the origin of the mitochondrial reprogramming in *Gls1*-deficient macrophage (Fig. 4a)[20], we performed an RNA sequencing (RNA-seq) analysis of PCMs stimulated by IL-4 *in vivo*. Metabolic pathway enrichment analysis highlighted down-regulation of oxidative phosphorylation and GSH synthesis KEGG pathways (i.e, NADP, folate and GSH metabolism) in resting and reparative Mac$^{\Delta Gls1}$ PCMs (Fig. 4b). Thus, to dissect the interplay between the mitochondrial metabolic repurposing and the perturbation in

antioxidant metabolism in Mac$^{\Delta Gls1}$ macrophages, we next performed topological analyses using CoMBI-T profiling[9], and compared predictions to DreamBio that allows direct computational KEGG pathway mapping. CoMBI-T and DreamBio profiling analyses featured a link between Mac$^{\Delta Gls1}$ PCM mitochondrial metabolic reprogramming and lower expression of TCA cycle and aspartate-arginino-succinate (AAS) shunt genes. These genes are interconnected to metabolism of glutamine *per se*, carbohydrates, hexosamine and fatty acids (Extended Data Fig. 4a and 4b). CoMBI-T predictions also revealed that the redox status of reparative Mac$^{\Delta Gls1}$ PCMs may connect to the one carbon cycle-centered module known to support the transsulfuration pathway (i.e, GSH synthesis) (Extended Data Fig. 4a). KEGG mapping with DreamBio offered an alternative visualization of the perturbed transcriptomic pathways in reparative *Gls1*-deficient macrophages and highlighted additional reactions that were not yet predicted (Extended Data Fig. 4b). For instance, in contrast to CoMBI-T, DreamBio analysis predicted downregulation of phosphogluconate dehydrogenase (*Pgd*) and malic enzyme (*Me1*) in reparative *Gls1*-deficient macrophages. These are two genes enconding enzymes that contribute to GSH salvage pathway through NADPH generation to efficiently supply reduced glutathione and maintain macrophage redox status (Extended Data Fig. 4b). Altogether, this unique approach helped to pinpoint the metabolic origin on how GLS1-dependent glutamine metabolism can integrate canonical mitochondrial reprogramming (i.e, TCA and AAS shunt) and non-canonical redox status (i.e, GSH synthesis and GSH salvage pathway) to support macrophage reparative function.

## Canonical glutamine catabolism does not potentiate efferocytosis

To validate predictions of topological analyses, we next scrutinized the utilization of glutamate into the canonical glutaminolysis pathway, which relies on glutamate dehydrogenase (GLUD1) to fuel α-ketoglutarate (α–KG) into the TCA cycle (Fig. 4a). Inhibition of GLUD1 with epigallocatechin gallate (EGCG) raised basal OCR in reparative control macrophages but was not sufficient to rescue *Gls1*-deficient macrophage phenotypes (Fig. 4c, **left panel**). Treatment with EGCG also raised efferocytosis and ATP production (Fig. 4c right panel and Extended Data Fig. 5a). Consistently, α–KG-dependent KDM6 and ten-eleven translocation dioxygenase 2 (TET2) activities were similar between control and Mac$^{\Delta Gls1}$ BMDMs (Extended Data Fig. 5b). Treatment of control and Mac$^{\Delta Gls1}$ BMDMs with dimethyl β–KG did also not rescue the inhibitory effect of *Gls1* deficiency on basal OCR (Extended Data Fig. 5c). Thus, the reduced glutamate levels in *Gls1*-deficient macrophages must impact non-canonical glutaminolysis pathways. To genetically validate these findings, we generated macrophage deficient for *Glud1* from mice lacking *Glud1* in hematopoietic cells (Extended Data Fig. 5d). In contrast to *Gls1* deficiency, higher basal OCR and maximal respiration response (Fig. 4d), ATP production rate (Fig. 4e) and efferocytosis (Fig. 4f) were measured in reparative *Glud1*-deficient macrophages. Thus, the reduced ATP production in *Gls1*-deficient macrophages is unlikely the consequence of reduced glutamate utilization into the canonical GLUD1-dependent glutaminolysis to fuel the TCA cycle.

## Non-canonical glutamine transamination supports efferocytosis

We next investigated how perturbation of glutamate production connects non-canonical AAS shunt and oxidant stress to mitochondrial function in *Gls1*-deficient macrophages through

pharmacological approaches and functional testing (Fig. 4a). Replenishment of the non-canonical GSH synthesis pathway with N-acetylcysteine (NAC) to prevent ATP leakage by limiting the $\gamma$-glutamyl futile cycle synthesis[7], had no effect on either OCR, ATP production or efferocytosis in $Mac^{\Delta Gls1}$ BMDMs (Fig. 4c and Extended Data Fig. 5a). Indeed, a role of this futile cycle was unlikely as we also observed similar amounts of the pyroglutamate intermediate (also known as PCA or 5-oxoproline) in $Mac^{\Delta Gls1}$ BMDMs (Extended Data Fig. 5e). In strong contrast, inhibition of the non-canonical aspartate aminotransferases ($GOT_s$)-dependent transamination with aminooxyacetic acid (AOA) reduced basal OCR, ATP production and this limited efferocytosis in control macrophages to the levels of reparative $Mac^{\Delta Gls1}$ BMDMs (Fig. 4c and **Extended Data 5a**). Treatment with AOA also inhibited efferocytosis during continued clearance of ACs in resolving control and $Mac^{\Delta Gls1}$ BMDMs (Extended Data Fig. 5f) or in reparative *Glud1*-deficient BMDMs (Fig. 4f). We validated these observations by showing that reduced expression of Got1 and Got2 by siRNA in BMDMs prevented the engulfment of ACs (Extended Data Fig. 5g). Thus, the reduced ATP production in *Gls1*-deficient macrophages is the consequence of reduced glutamate utilization into the non-canonical transaminase-dependent malate-aspartate shuttle.

## Glutaminolysis acts through AAS shunt to support efferocytosis

The non-canonical transaminase-dependent malate-aspartate shuttle is known to not only maximize the production of ATP but also the number of NADPH molecules by being nested to the AAS shunt[7]. Consistently, we also observed a decrease in NAD(P)H levels in reparative $Mac^{\Delta Gls1}$ BMDMs that was recapitulated by GOT inhibition with AOA (Fig. 4g). To substantiate further these connections, we next measured the ratio between NADPH/NADP and GSH (reduced glutathione)/GSSG (glutathione disulfide), known to scavenge ROS[7]. As expected, a decrease in the NADPH/NADP ratio was strongly correlated to the GSH/GSSG ratio in $Mac^{\Delta Gls1}$ PCMs (Extended Data Fig. 5h) leading to higher ROS levels (Extended Data Fig. 5i). Supplementation with GSH to bypass this GSH salvage pathway defect raised basal OCR levels, ATP and NAD(P)H production and efferocytosis in reparative $Mac^{\Delta Gls1}$ BMDMs almost to the levels of control macrophages (Extended Data Fig. 5j to 5l). In contrast, overexpression of glutathione-disulfide reductase (GSR) did not increase but rather slightly attenuated NAD(P)H levels and had no impact on efferocytosis in reparative $Mac^{\Delta Gls1}$ PCMs (Fig. 4h). Thus, we reasoned that impaired NADPH generation rather than NADPH consumption by GSH recycling was involved in the defective efferocytosis of *Gls1*-deficient macrophages. To validate this hypothesis, we overexpressed NADPH-producing malic enzymes (ME) involved in the malate-pyruvate cycling pathway, nested to the non-canonical transaminase-dependent malate-aspartate shuttle (Fig. 4a). Overexpression of ME1 and ME2 using lentiviral particles not only restores the NAD(P)H levels in reparative $Mac^{\Delta Gls1}$ PCMs but also their efferocytic capacity (Fig. 4h). Altogether, these findings pinpoint how glutaminolysis couples oxidative stress buffering to OXPHOS through non-canonical glutamine transamination metabolism.

## Glutaminolysis controls apoptotic corpses engulfment

When compared to control PCMs, *Gls1*-deficient cells had similar transcriptional regulation of genes encoding proteins involved in the sensing of soluble mediators attracting the

phagocytes to ACs ('smell' or 'find-me' signals), the direct contact and recognition of ACs by ligand-receptor interactions ('taste' or 'eat me' signals) and the corpse internalization and processing ('ingestion' and 'digestion' processes) (Extended Data Fig. 6a). Downregulation of various actin rearrangement/polymerization genes such as small GTPases Rac1 and Cdc42 or the newly identified Rac1 transcriptional regulator GTP-exchange factor (GEF) Dbl has recently been linked to the metabolic adaptation during continual efferocytosis[4,10]. Although a slightly down regulation of Cdc42 mRNA expression was observed in reparative *Gls1*-deficient macrophages, this was not observed for Rac1 (Extended Data Fig. 6b) and Dbl expression (Extended Data Fig. 6c). In contrast, some nucleotide metabolism enzymes such as *Nme1*, *Nme6* or *Suclg1*, known to encode enzymes modulating GEF activity through spatiotemporally controlled GTP production, were downregulated in *Gls1*-deficient macrophages (Extended Data Fig. 6d). Nevertheless, overexpression of these enzymes had little effect on efferocytosis (Extended Data Fig. 6e). Thus, we reasoned that glutaminolysis must control the efferocytic response through post-transcriptional regulation. Treatment of *Gls1*-deficient macrophages for 15min with cytochalasin D, an actin polymerization inhibitor, indicated that the decrease in AC efferocytosis in $Mac^{\Delta Gls1}$ BMDMs was due to a defect in AC internalization (Fig. 5a). These findings suggest a post-transcriptional defect in the dynamic rearrangement of actin to engulf corpse during phagosome sealing[6]. This is an energy-intensive process, as actin polymerization and depolymerization steps require an ATP-dependent nucleation phase of new actin filaments (Extended Data Fig. 6b) and this process is regulated by RAC1 and CDC42 activities[21]. We indeed observed a slower polarization of G- to F-actin in reparative $Mac^{\Delta Gls1}$ macrophages (Fig. 5b) along with reduced activity of CDC42 and a trend for RAC1 (Extended Data Fig. 6f and 6g). Consistently, transmission electron microscopy revealed less membrane ruffling surrounding the $Mac^{\Delta Gls1}$ BMDMs (Fig. 5c). Phalloidin immunostaining, 10 min after efferocytosis, also revealed a general decrease in the amount of F-actin staining at the leading edge of membrane ruffle formation surrounding the ACs, indicative of reduced actin polymerization in efferocytic $Mac^{\Delta Gls1}$ phagocytes (Fig. 5d). Blocking the energy-intensive actin rearrangement with NSC-23766, a RAC1 inhibitor or ML141, a CDC42 inhibitor recapitulated the efferocytic defect observed in reparative and resolving $Mac^{\Delta Gls1}$ macrophages (Extended Data Fig. 6h and 6i). This effect appears independent of the post-transcriptional regulation of RAC1 by the Drp1-mediated mitochondrial fission[3], as reduced efferocytosis in $Mac^{\Delta Gls1}$ BMDMs was still observed after Drp1 inhibition with MDIVI-1 treatment (Extended Data Fig. 6h and 6i). In contrast, we validated the role of non-canonical glutamine transamination pathway in the energy-intensive engulfment process by blocking the AAS shunt with AOA, which blunted RAC1 and CDC42 activities (Extended Data Fig. 6f and 6g) and reduced F-actin immunostaining to the same level after AC engulfment in reparative control and $Mac^{\Delta Gls1}$ BMDMs (Fig. 5d). Finally, to link the defect in mitochondrial ATP generation to the high-energy requirement of cytoskeletal rearrangements in reparative $Mac^{\Delta Gls1}$ macrophages, we blocked the transport of ATP produced from OXPHOS to the cytoplasm by targeting the mitochondrial carrier adenine nucleotide translocator (ANT) with the carboxyatractyloside (CATR) inhibitor. A 15min treatment with this inhibitor was sufficient to dose dependently reduce efferocytosis in control macrophages with minimal impact on reparative $Mac^{\Delta Gls1}$ BMDMs abolishing the difference between genotypes at the highest concentration (Fig. 5e). Consistently, ANT

inhibition for 15 min with CATR limited the amount of F-actin staining around the phagocytic cup in control macrophages almost to the levels of reparative $Mac^{\Delta Gls1}$ BMDM (Fig. 5f). Thus, our results reveal that glutaminolysis and non-canonical transaminase pathways are essential to maximize the number of ATP molecules produced in mitochondria and meet the demand for high-energy actin polymerization that facilitates the process of corpse engulfment (Extended Data Fig. 7).

## Discussion

Macrophages require substantial amount of nutrients after ingestion of ACs (i.e, efferocytosis) to maintain normal tissue function[6]. We and others have demonstrated that efferocytes can adapt their metabolism to face cholesterol and fatty acid overload during this process[11,22–24]. Increased glucose uptake preceding AC engulfment could also prime continued AC clearance[10]. We now uncover that GLS1-dependent glutaminolysis is required to optimize AC clearance upon IL-4 stimulation or continued AC uptake by efficiently reprogramming macrophage metabolism. Indeed, conversion of glutamine through non-canonical transaminase pathways couples oxidative stress buffering to ATP production to meet the demand for high energy actin dynamics and cytoskeletal rearrangements.

Glutamine is considered a conditionally essential amino acid because of its role during metabolic stress, including injury[7,8], and predicted macrophage activation profiles in aortas of atherosclerotic mouse models[25]. However, the fundamental link between GLS1 and efferocytosis in this setting remains to be elucidated. Strikingly, despite enhanced glutamine utilization in the aortas of atherosclerotic mice, we observed impaired glutamate conversion and reduced *Gls1* expression, reflecting perturbed glutaminolysis. In our mouse and human datasets, we also observed that *Gls1* expression within plaques was positively associated to canonical alternative polarization markers suggesting that glutaminolysis, rather than glutamine uptake could predict macrophage polarization. *Gls1* expression also negatively correlated with necrotic cores.

Modulation of glutamine metabolism can lead to strikingly different phenotypes in immune cells. For instance, it has recently been suggested that glutaminolysis could promote mTORC1 signaling during Th1 differentiation[26]. In the current setting, we did not observe perturbations of glycolysis or downstream mTOR signaling pathways in glutaminolysis deficient macrophages. Because an enhanced transcriptomic signature of genes involved in amino acid catabolism in *Gls1*-deficient cells was observed, we investigated the metabolism of specific amino acids that has recently emerged to control macrophage effector functions. For example, BC-AAs cause itaconate accumulation, a hallmark of macrophage proinflammatory response[27,28]. The group led by Tabas et al. have also recently reported that the metabolism of AC-derived arginine or ornithine to putrescine is required for continual efferocytosis by a mechanism involving cytoskeletal rearrangements[4], and potentially linked to mitochondrial fission[3]. However, impaired macrophage glutaminolysis likely occurs independently of the aforementioned amino acid pathways as similar levels of BC-AAs and putrescine were observed in *Gls1*-deficient macrophages. Furthermore, inhibition of BCAT or ornithine supplementation did not rescue the defective efferocytosis of these cells. Thus, *Gls1*-deficient cells may impact amino acid catabolism as an attempt

to compensate for the loss of glutamate generation, but this was unlikely the cause of the defective efferocytosis in these cells.

Glutamine can be converted through glutamate dehydrogenase (GLUD1) or non-canonically into GSH synthesis or via transaminases. Canonical glutaminolysis could support α–KG generation to orchestrate the jumonji domain containing-3 (Jmjd3, KDM6B)-dependent epigenetic reprogramming of alternatively activated macrophages[29]. However, we did not observe perturbations of α–KG-dependent epigenetic activity and α–KG supplementation did not rescue the defective efferocytosis observed in *Gls1*-deficient macrophages. Unexpectedly, *Glud1* deficiency also exhibited an opposite efferocytosis phenotype relative to *Gls1* deficiency suggesting that the reduced glutamate generated in *Gls1*-deficient macrophages impacted non-canonical glutaminolysis pathways. Consistently, high-throughput transcriptional and metabolic profiling indicated that defective glutaminolysis in macrophages predominantly perturbed downstream non-canonical GSH synthesis and transaminase pathways. Mechanistic studies further confirmed that glutaminolysis was essential to limit oxidant stress but also to support mitochondrial OXPHOS and ATP production in resolving and reparative macrophages.

The perturbation of non-canonical GSH synthesis in macrophages with defective glutaminolysis may have pleiotropic effects. First, it could impact mitochondrial redox status that has been previously shown to metabolically program macrophage effector functions[16,17]. However, we excluded a causal role of mitochondrial ROS in the metabolic reprogramming and defective efferocytosis of *Gls1*-deficient macrophages. It has been previously suggested that glutamate oxidation by complex I can be used to direct the ETC in the forward direction independently of the redox state of CoQ and $\Delta\psi m$[30,31]. Thus, the enhanced mitochondrial ROS production in *Gls1*-deficient macrophages is unlikely the consequence of the perturbed non-canonical GSH synthesis in these cells but rather a ‘by-products’ of the defective OXPHOS and ATP generation and is not responsible for their defective efferocytosis. A second scenario involved ATP leakage through the γ-glutamyl futile cycle synthesis, which is part of non-canonical GSH synthesis pathway[7]. However, we also excluded a perturbation of this pathway in *Gls1*-deficient macrophages. Finally, the lower GSH/GSSG ratio that was associated with a higher oxidant stress in macrophages with defective glutaminolysis rather suggested perturbation in the recycling of GSH to GSSG, which depends on NADPH-consuming or producing enzymes. Although GSH supplementation rescued the defective efferocytosis of *Gls1*-deficient macrophages, overexpression of GSR, the rate-limiting enzyme of GSH recycling that consumes NADPH, did not. Further studies will be required to pinpoint whether the beneficial effect of GSH in reparative *Gls1*-deficient macrophages involves enhanced respiratory chain efficiency by limiting CoQ oxidation and subsequent mitochondrial supercomplex assembly[32,33], or reduced NADPH consumption, which ‘energy value’ can be roughly estimated at between 2.5 and 3.5 ATP equivalents for purposes of comparing energy inputs and outputs of metabolic pathways[34]. Nevertheless, the mechanism by which GSH rescued efferocytosis in *Gls1*-deficient macrophages was associated with its ability to improve OXPHOS, ATP generation and NAD(P)H levels.

The transaminase-dependent malate-aspartate shuttle is nested to the AAS shunt and requires glutamate to regenerate NADH, which is used to transfer electrons to the ETC. This is required to maximize the number of ATP molecules produced in mitochondria and favor NADPH production through ME-dependent malate-pyruvate cycling pathway to support GSH salvage pathway[7]. Consistently, all markers of these pathways were downregulated in *Gls1*-deficient macrophages along with reduced activity of mitochondrial complex I and II. The central role of ATP produced within mitochondria after glutamate is channeled into the malate-aspartate shuttle by aspartate aminotransferase (GOT)-dependent transamination in efferocytes was ultimately highlighted by directly targeting GOTs and mitochondrial complex II and III. Finally, overexpression of ME1 and ME2 not only restored NAD(P)H levels but also the defective efferocytic capacity of reparative *Gls1*-deficient macrophages. Thus, defective non-canonical transaminase pathway in *Gls1*-deficient macrophages reveals how glutaminolysis couples oxidative stress buffering to OXPHOS and ATP production, which is linked to the ability of these pathways to power cells with the reducing equivalents necessary to detoxify ROS and support the TCA cycle anapleurosis required for efficient efferocytosis.

The high-energy demand for cytoskeletal rearrangements during efferocytosis has previously been suggested, but the underlying mechanisms remain poorly understood[2]. Actin remodeling is an energy-intensive process involving polymerization and depolymerization steps and formation of membrane ruffling for AC recognition and internalization that can be metabolically regulated by transcriptional[4,10], or post-transcriptonal modifications[3,24]. However, we did not identify a specific genetic signature that could link glutaminolysis to efferocytosis including the one targeting Rac1 and Cdc42, which are key regulators of this process. For instance, we did not observe a role for the recently identified transcriptional regulation of Rac1 by GTP-exchange factor Dbl[4]. Thus, defective efferocytosis and actin remodeling was rather the consequence of post-transcriptional regulation in macrophage with defective glutaminolysis. Along with reduced ATP production in *Gls1*-deficient macrophages, we indeed observed impaired actin polymerization and reduced Cdc42 and Rac1 activities. This was ultimately associated with defective F-actin polymerization in membrane ruffles after the ingestion of ACs that was recapitulated by targeting the non-canonical transaminase pathway. This process required the ANT-dependent transport of ATP from mitochondria through the cytoplasm. Thus, several complementary mechanisms exist to sustain an efficient successive clearance of ACs. We now identified that macrophage glutaminolysis supports the high-energy demand for F-actin remodeling during this process.

Collectively, our results reveal a dependence on transaminases for metabolism of the glutamine carbon skeleton during key macrophage effector functions that are required for tissue repair. Mechanistically, these reactions orchestrate ATP generation through the ETC in the presence of IL-4 or during continued AC clearance. These findings support the larger concept that any process that compromises the metabolic reprogramming and ATP production of efferocytes will likely result in dire pathologic consequences. Conversely, therapeutic interventions to enhance macrophage glutaminolysis and boost efferocytosis have the potential to subvert maladaptive inflammation and tissue necrosis.

# Methods

## Human atherosclerosis

Tissue collection was part of the Maastricht Pathology Tissue Collection (MPTC) and further storage and use of the tissue was in line with the Dutch Code for Proper Secondary use of Human Tissue and the local Medical Ethical Committee (protocol number 16-4-181).

Carotid arteries were collected from 22 symptomatic male patients undergoing carotid endarterectomy (CEA) in the Maastricht human plaque study (MaasHPS) (72.9 ± 6.3 years old) as previously described[35]. Formalin-fixed, paraffin embedded (FFPE) 5mm-segments were alternated with frozen segments for RNA isolation. Two independent pathologists then classified FFPE segments in a blind fashion as fibrous cap atheroma with or without intraplaque hemorrhage (16 stable segments and 27 unstable segments, respectively) according to haematoxylin-eosin (HE) staining. Stable and unstable snap-frozen segments were used for further microarray analysis. Snap-frozen segments were pulverized and 5-20mg of material was subjected for transcriptomics. RNA isolation was performed by Guanidium Thiocyanate extraction and further purified with the Nucleospin RNA II kit (Macherey-Nagel GmbH&Co). RNA quality and integrity were determined using the Agilent 2100 Bioanalyzer. Biotinylated cRNA was prepared with Illumina TotalPrep RNA Amplification Kit (Ambion, TX, U.S.A) and 750ng cRNA per sample was used for hybridization (Illumina Human Sentrix-8 V2.0, Beadchip®). Scanning was performed on the Illumina Beadstation 500 (Illumina, CA, U.S.A) and image analysis was done using the Illumina Beadstudio v3 Gene expression software. A total of 22,184 human transcripts were analyzed in R Bioconductor lumi package.2 Firstly, a variance stabilizing transformation, which is incorporated in the lumi package, was performed. Secondly, Robust Spline Normalization (RSN) algorithm in lumi package was applied to normalize the data. Differential gene expression analysis was done by using the function lmFit() provided in Limma R package on preprocessed transcriptomics data.3

The 88 adjacent tissue sections were phenotyped extensively for plaque size, necrosis, inflammation (CD68, CD3, arginase, iNOS), SMCs (αSMA), collagen (Sirius red) and angiogenesis (CD31+ microvessel density, newly formed CD105+ microvessels, αSMA+ mature microvessels, Lyve+ lymphatic density). Pearson correlation analysis was performed to assess the association between gene expression and plaque phenotypical traits.

## Mice

$Gls1^{fl/fl}$ mice were kindly provided by Pr. Stephen Rayport (Glstm2.1Sray/J deposited at The Jackson Laboratory) and have been crossed to $Lyz2^{Cre}$ mice (B6.129P2-Lyz2tm1(cre)Ifo/J, The Jackson Laboratory) or $Mx1^{cre}$ mice (B6.Cg-Tg(Mx1-cre)1Cgn/J) and brought on Apoe-deficient genetic background (B6.129P2-ApoEtm1Unc/J). $Mx1^{cre}$ mice (B6.Cg-Tg(Mx1-cre)1Cgn/J) were also crossed to C57BL/6 Glud1 floxed mice (kindly provided by Pr. Pierre Maechler). For each experiment, co-housed littermate male and female controls were used between eight and fourteen weeks of age. Animal protocols were approved by the Institutional Animal Care and Use Committee of the French Ministry of Higher Education and Research and the Mediterranean Center of Molecular Medicine

(Inserm U1065) and were undertaken in accordance with the European Guidelines for Care and Use of Experimental Animals. Animals had free access to food (chow diet A04, Safe$^{R}$) and water and were housed in a controlled environment with a 12-hour light–dark cycle, constant temperature (21.7-22.8°C) and relative humidity (50-60%). Water and cages were autoclaved. Cages were changed once weekly, and the health status of the mice was monitored using a dirty bedding sentinel program. Hyperlipidemia was induced by feeding the mice with a Western diet (TD88137, Ssniff) for 12 weeks.

### Poly(I:C) induction

Mx1$^{cre}$ mice were i.p. injected with 1mg/mL poly(I:C) three times every two days. Mice were then used for experimentation 3 weeks later.

### IL-4c *in vivo* treatment

Mice were i.p. injected with IL-4 complexed to anti-IL-4 mAb (IL-4c; containing 5 μg of IL-4, PeproTech, and 25 μg of anti-IL-4 clone 11B11, BioXcell). 36 hours later, PCMs were collected and analyzed by flow cytometry.

### Cell culture, PCMs and BMDMs generation

BM cells were harvested from mouse femur and tibia and differentiated in the presence of recombinant mouse M-CSF (20 ng/ml; Miltenyi) in complete RPMI 1640 medium (Corning) containing 10mM glucose, 2mM L-glutamine, 100U/ml of penicillin/streptomycin, and 10% FBS for 7 days at 37°C and 5% CO2. Peritoneal Cavity Macrophages (PCMs) were obtained by peritoneal lavage with 5ml of PBS.

### Cell treatments

At day 7 BMDMs were collected, plated and activated overnight as indicated. Peritoneal cells were obtained by peritoneal lavage with 5ml of PBS. Cells were plated and cultured overnight in complete RPMI 1640 medium (Corning) containing 10mM glucose, 2mM L-glutamine, 100U/ml penicillin/streptomycin, and 10% FBS at 37°C and 5% CO2. Cell were incubated overnight with the following treatments: IL-4 (20ng/mL, Peprotech), AOA (200μM, Sigma), Dimethyl-α-ketoglutarate (1mM, Sigma), EGCG (100μM, Sigma), GSH (10mM, Sigma), L-ornithine (1mM, Sigma), BCATc inhibitor (20μM, Cayman Chemical), Gabapentin (10μg/mL, Sigma), 3NPA (1.68mM, Sigma), Antimycin A (0.1μM, Sigma), Tempol (4mM, EMD Millipore), mitoquinol (200nM, Cayman Chemical), NAC (10mM, Sigma), MDIVI-1 (10μM, Sigma), NSC23766 (50μM, EMD Millipore) or ML141 (10μM, EMD Millipore) (Supplemntary Table. 2).

### siRNA transfection

Cells were transfected with Got1/Got2 siRNA (L-043492-01-0005 and L-043495-01-0005, Dharmacon) or control siRNA (D-001810-01-05, Dharmacon) (referred to as Scbl) at 30 nM using Lipofectamine RNAiMAX (Life Technologies), according to the manufacturer's instructions.

### Lentivirus overexpression

Cells were spin-transfected for 90min at 1,300 g with Gls1, lentivirus (LVM(VB200119-1197bpk)-C, Vectorbuilder), Nme1 (Vector ID: VB200120-1064ucb, Vectorbuilder), Nme6 (Vector ID: VB200120-1213tjc, Vectorbuilder), Suclg1 (Vector ID: VB200120-1214hxx, Vectobuilder), Me1 (Vector ID: VB201125-1076tsb, Vectorbuilder), Me2 (Vector ID: VB201125-1253dre, Vectorbuilder), Gsr (Vector ID: VB201125-1094mzr, Vectorbuilder) or control lentivirus (LVM(VB200120-1215tyv)-C, Vectorbuilder) (referred to as Scbl) and used at MOI 10. Same protocol was used for AOX overexpression using Lenti-ONE AOX viral particles (GEG Tech) and Lenti-ONE gfp (referred as Empty) viral particles (GEG Tech) at MOI 5. After 6 hours, cells were washed, and the media replaced with fresh media for 48 hours before treatment.

### Western Blotting

LPMs were cell-sorted and then lysed in RIPA buffer containing protease inhibitors cocktail (ThermoFisher) and agitated for 1 hour at 4°C before centrifugation at 20,000 g for 10min at 4°C. Protein samples were resolved on 10% SDS-PAGE gels and were then transferred onto polyvinylidene difluoride membrane using a wet transfer system. Membranes were blocked in 5% (w/v) BSA in Tris-buffered saline-Tween for one hour at room temperature. Membranes were then incubated with primary antibody (anti-Glud1 or anti-Gls1 antibodies (Abcam)) followed by the appropriate horseradish peroxidase-conjugated secondary antibody. Anti α-actin mAb (Santa Cruz) was used as loading control. Proteins were detected by substrate HRP (Sigma). Antibody validations were performed by suppliers and antibodies were used according to manufacturer's instructions.

### Analysis of atherosclerotic plaque

Mice were sacrificed and slowly perfused with 10ml of ice-cold PBS. The hearts and aortas were carefully excised and fixed in 4% paraformaldehyde containing 30% sucrose. The aortas were stained with Oil Red O (Sigma-O0625) to evaluate plaque neutral lipid content. The hearts were embedded in OCT compound (Gentaur) and stored at −80°C before analysis. 10μm cryosections of the aortic sinus were prepared. Oil Red O staining was used to detect neutral lipid content in the plaque combined with a haematoxylin/eosin staining to analyse tissue architecture. Plaque macrophages were visualized using purified anti-CD68 mAb (clone FA-11, AbD Serotec). Anti-rat Alexa Fluor 488-conjugated antibody (A-11006, Life technologies) was used for detection of CD68 staining. For analysis of plaque macrophage proliferation, anti-Ki67 PE conjugated mAb (clone 16A8, BioLegend) was used. Nuclei were revealed with DAPI counterstaining (2μg/ml). TUNEL staining was performed using the DeadEnd™ Fluorometric TUNEL System (Promega). Plaque area quantification were measured with ImageJ software.

### Echography

Male mice were fully anesthetized with 1.5% Isoflurane before and during ultrasound scanning. Before all ultrasound scanning, the hair of the mouse chest wall was carefully removed, and warm ultrasound transmission gel was liberally applied to ensure optimal

image quality. Echocardiography was performed using a high-frequency Vevo2100 (Visualsonics)-imaging.

### Transmission Electronic Microscopy

Cells were observed with transmission electron microscopy (TEM) for ultrastructural analysis. Cells were fixed in a 1.6 % glutataraldehyde solution in 0.1 M sodium phosphate buffer at room temperature (RT) and stored overnight at 4°C. After three rinsing in 0.1 M cacodylate buffer (15 min each), cells were postfixed in a 1 % osmium tetroxide and 1 % potassium ferrocyanide solution in 0.1 M cacodylate buffer for 1 hour at RT. Cells were subsequently dehydrated in a series of acetone baths (90 %, 100% three times, 15 min each) and progressively embedded in Epon 812 resin (acetone / resin 1:1, 100 % resin two times, 2 hours for each bath). Resin blocs were finally left to harden in a 60 °C oven for 2 days. Ultrathin sections (70 nm) were obtained with a Reichert Ultracut S ultramicrotome equipped with a Drukker International diamond knife and collected on 200 mesh copper grids. Sections were stained with lead citrate and uranyl acetate. TEM observations were performed with a JEOL JEM-1400 transmission electron microscope, equipped with a Morada camera, at a 100kV acceleration voltage.

### *In vitro* efferocytosis analysis

BMDMs and PCMs were generated and stimulated as described above. To generate apoptotic cells (ACs), thymii from C57BL/6J mice were harvested and mechanistically dissociated, filtered on 100μm nylons (Falcon), pelleted and resuspended in RPMI medium supplemented with 10% FBS. Apoptosis was induced by UV exposure at 312nm for 10min and cells were maintained in culture for an additional 2 hours. This method results in 70-90% apoptosis[23]. ACs were labelled with CellTrace™ Violet Cell Proliferation kit (ThermoFisher) according to the manufacturer's instructions. Fluorescent ACs were washed twice with PBS before use. For one round efferocytosis: stained ACs were added at a 5:1 ratio on plated macrophages for 45min. For two rounds efferocytosis: unlabelled ACs were added at a 5:1 ratio on plated macrophages for 45min. Cells were then washed 3 times and macrophages were incubated for 1h. Stained ACs were then added at a 5:1 ratio on macrophages for 45min. Cells were washed 3 times and macrophages were stained and analysed for AC content and activation markers by flow cytometry. In some experiment, macrophages were treated for 15 min prior efferocytosis with cytochalasin D (5μM, Sigma). For Seahorse extracellular flux analysis ACs were injected directly, before drug treatment, during the assay.

### *Escherichia Coli* phagocytosis assay

BMDMs were loaded with 1 μg of Fluorescein-labeled *Escherichia Coli* K12 Bioparticles (Fisher) for 30 minutes at 37°C and intracellular fluorescence of engulfed particles was calculated after quenching of the extracellular probe by trypan blue according to the manufacturer's instruction.

### Immunofluorescence

BMDMs and ACs were generated and stimulated as described above. ACs were stained with CellTrace™ CFSE (Invitrogen) for 30min prior to one round efferocytosis. After 15min of efferocytosis, BMDMs were washed with a 37°C heated medium and fixed for 10min at 37°C with 4% paraformaldehyde culture medium. Cells were then saturated for 30min in PBS 10% FBS. Cells were incubated for 30min with Texas Red™-X Phalloidin (Invitrogen). Cells were then washed thoroughly, and coverslips were mounted with aqueous glue. Sections were observed the following day by fluorescent microscopy.

### *In vivo* efferocytosis analysis

ACs were generated as described above. Mice were i.v injected with $2*10^7$ stained ACs and 1 hour later, the spleen and liver were collected and analysed by flow cytometry.

### *In vitro* flow cytometry analysis

Cells were stained for 25 min at 4°C protected from light. For flow cytometry analysis the following list of antibodies was used: MitoSOX™ Red (ThermoFisher), ROS (Thermofisher, CM-H2DCFDA), CD206 PerCp-Cy5.5 conjugated (clone C068C2, BioLegend), MerTK PE conjugated (clone 2B10C42, BioLegend), CD115 PE conjugated (clone AFS98, eBioscience), CD64 Brillant Violet 421 conjugated (clone X54-5/7.1, BioLegend), F4/80 Pe-Cy7 conjugated (clone BM8, BioLegend), Annexin V (Biolegend). Antibody validations were performed by suppliers and antibodies were used according to manufacturer's instructions. Cells were then washed, centrifuged and data were acquired on BDFACSCanto flow cytometer. FSC/SSC gating was used to exclude dead cells and debris followed by FSCA/FSCH to select singlets. Gating strategy for all viable cells have been described in the manuscript. Data collection was performed using FACS DIVA software and analysis was performed using FlowJo software (Tree Star).

### Intracellular flow cytometry

For all intracellular stainings: Phospho-S6 Ribosomal Protein (Ser235/236) PE conjugated (clone D57.2.2E, Cell signaling), c-Myc PE Conjugate (Clone D84C12, Cell signaling). Cells were removed from media, stained for surface, fixed, then stained for intracellular proteins using Foxp3 Transcription Factor Fixation/Permeabilization kit (BD biosciences).

### *In vivo* flow cytometry analysis

Cells were collected from spleen, peritoneal cavity, bone marrow, liver and brain. Tissues were collected after cardiac PBS perfusion. Splenocytes were extracted by pressing spleens through a stainless-steel grid. Peritoneal and bone marrow leukocytes were harvested by PBS lavage. Liver and brain were cut in small piece and digested for 30min with HBSS medium containing 1,5mg/mL collagenase D (Roche) at 37°C. For liver and microglia preparation, an additional purification step was performed by Percoll gradient. Single-cell suspension was submitted to red blood cell lysis, filtration, and centrifugation for 5min at 400 g. Cell suspensions were stained with the appropriate antibodies for 30min on ice protected from light. The following antibodies were used for macrophage flow cytometric analysis: CD11b Brillant Violet 510 conjugated (clone M1/70, BioLegend),

CD115 PE conjugated (clone AFS98, eBioscience), CD45 APC-Cy7 conjugated (clone 30-F11, BD Biosciences), CD64 Brillant Violet 421 conjugated (clone X54-5/7.1, BioLegend), CD11c APC conjugated (clone N418, BioLegend), F4/80 Pe-Cy7 conjugated (clone BM8, BioLegend), CD206 PerCp-Cy5.5 conjugated (clone C068C2, BioLegend), CD301 FITC conjugated (clone ER-MP23, Bio-Rad). Cells were then washed, centrifuged and data were acquired on BDFACSCanto flow cytometer. NAD(P)H levels were assessed by endogenous fluorescence emission within the 420-480nm range. Data collection was performed using FACS DIVA software and analysis was performed using FlowJo software (Tree Star) as described above.

## Seahorse extracellular flux analysis

For extracellular flux assay, $1 \times 10^5$ BMDMs or LPMs were plated in a Seahorse Bioscience culture plate. Cells were then incubated overnight with different drugs and metabolites. OCR and ECAR was measured by an XF96 Seahorse Extracellular Flux Analyzer following the manufacturer's instruction. In the seahorse assay, cells were treated with oligomycin (1μM), FCCP (1.5μM), rotenone (1μM) and antimycin A (0.1μM). ATP production is measured after injection of oligomycin and calculated using the Seahorse XF report generator. Each condition was performed in 3 replicates.

## RNAseq

PCMs were obtained by lavage as described above. Then cells were stained with CD64 Brilliant Violet 421 conjugated (clone X54-5/7.1), ICAM-2 Alexa Fluor 647 conjugated (clone 3C4(MIC2/4)) and CD115 PE conjugated (clone AFS98). These antibodies allow us to separate the two subsets of peritoneal macrophages with only the major one expressing ICAM-2[36]. Cells were cell sorted on BD FacsAria flow cytometer. Total RNA was extracted with RNeasy Mini Kit (Qiagen) according to the manufacturer's protocol and quality was assessed by Nanodrop (Ozyme). Library constructions were conducted as described previously[9]. Libraries were sequenced at the Centre for Applied Genomics (SickKids, Toronto) using a HiSeq 2500 (Illumina).

## Integrated network analyses

Network-based integration of metabolite and gene expression datasets was conducted using Shiny Gam as previously described[9]. We also developed *DreamBio*, a complementary topological tool for Integrated Network Analysis mapped into KEGG pathway. The same strategy than Shiny Gam was used[9] (https://artyomovlab.wustl.edu/shiny/gam/), except that GEPHI GEXF (graph exchange format) was converted from KGML to be analyzed through Sigma library, which is dedicated to graph drawing. Up and down regulated metabolic genes based on p values calculated with Phantasus[9], were mapped into models maintaining all essential KEGG pathway attributes. DreamBio will become soon freely available at https://biotest.hematometabolism.science/.

## Fluxomics

Metabolite extraction of BMDMs was performed on 2.5 million cells per well using 70°C aqueous 70% ethanol as described previously[37]. Briefly, [$^{13}$C]-Glutamine (1mM) was added

on free-glutamine media cells for 4 hours. At collection, cells were placed immediately on ice, the media was removed, and cells were washed three times with ice-cold PBS to remove residual media. Intracellular metabolites were extracted twice with hot ethanol. For LCMS, samples where dried under nitrogen flow and reconstituted in a milliQ water/acetonitrile (1:1) mixture for injection using a UPLC Acquity (Waters) separation system coupled with a Xevo G2 ToF (Waters). Compounds were ionized using an electrospray ionization source in negative mode. Data processing was performed in MATLAB (Mathworks, Inc.) using a custom-made in-house protocol. Compound identification was performed using both retention time of authentic standards and accurate mass with an accepted deviation of 0.005 Da. Raw data was converted to netCDF format using Chemstation (Agilent), before processing in MATLAB R2014b (Mathworks, Inc.) using PARADISe software. All MS sample processing and analysis were performed by MS-Omics, Inc. (Copenhagen, Denmark).

### Metabolomics

Metabolomics analyses were performed at CriBioM as previously described[38]. Briefly, control and Gls1-deficient BMDMs were treated with or without 20ng/mL IL-4 as indicated in the figure legends. Metabolites were extracted by exposing cells to cold methanol and analyzed by LC-MS.

### Typhoon™ Biomolecular Imager

2μCi of [$^{14}$C]-labelled glutamine were i.v. injected and mice were sacrificed 15 minutes later. Aortas were harvested and the associated adipose tissue was carefully dissected and removed. Imaging for [$^{14}$C]-labelled glutamine was performed on Typhoon™ Biomolecular Imager (Amersham). Whole mount staining with Oil Red O paralleled this analysis on the same samples.

### Thin-Layer Chromatography (TLC)

Aortic tissues were homogenized with 5% HClO4 solution and the radioactivity incorporated in this extract was measured before being dropped on silica-gel POLYGRAM precoated TLC sheets (Sigma). Separation of $^{14}$C glutamine and the $^{14}$C glutamine-derived glutamate was achieved in hexane/diethylether/formic acid (80:20:1 v/v/v) running buffer. The radioactivity was quantified and expressed as a percentage of ingested radioactivity.

### [$^{3}$H]-Thymidine incorporation

BMDMs were generated and stimulated as described above. The day before the experiment, cells were stimulated overnight with IL-4 (20ng/μL). [$^{3}$H]-Thymidine (1μCi) was added on cells in regular media for 2 hours. Cells were collected, centrifuged, washed with PBS, and resuspended in NaOH (0.1N)/SDS (0,1%) before adding scintillation.

### Plasma cholesterol and triglycerides content

Plasma cholesterol and triglyceride content were measured with LabAssayTM Cholesterol (Sobioda) and Triglycerides Reagent (Diasys) according to the manufacturer’s protocol.

### Glutamine/glutamate and GSH/GSSG measurements

Commercially available kits Glutamine/Glutamate-Glo™ Assay (Promega) and GSH/GSSG-Glo™ Assay (Promega) were used in accordance with the manufacturer's instructions.

### Complex I/II activity assay

Enzyme Activity Assay kit (ab109721 and ab109908) was determined according to the manufacturer's instruction.

### Rac1 and Cdc42 activity assay

Rac1 G-LISA Activation Assay Kit (Cytoskeleton BK128) and Cdc42 G-LISA Activation Assay Kit (Cytoskeleton BK127) was used according to the manufacturer's instructions.

### G-Actin/F-Actin assay

G-Actin/F-Actin activity was determined with G-Actin/F-Actin In Vivo Assay Biochem Kit (Cytoskeleton) according to the manufacturer's instructions.

### Actin polymerization assay

Actin polarization activity was determined with Actin Polymerization Biochem Kit (Cytoskeleton) according to the manufacturer's instructions.

### KDM6 and Tet2 activity assay

Tet2 and KDM6 activities were determined with MethylFlash Global DNA Hydroxymethylation (5-hmC) ELISA Easy Kit (Epigentek) and KDM6A/ KDM6B Activity Quantification Assay Kit (Abcam), respectively according to the manufacturer's instructions.

### IL-10 Secretion

IL-10 concentration in supernatant was measured using Mouse IL-10 Duoset ELISA kit (R&D) according to the manufacturer's instruction.

### Real-Time qPCR

Total RNA was isolated and cDNA was synthesized for real-time qPCR analysis. Gls1 (F: GCACATTATTCACCCGGTAACC; R: CTGCCCACCCACCATCC), Mertk (F: AAAGGTCCCCGTCTGTCCT, R: CCATCAAAACCAGGGACCC), Timd4 (F: AAAGGGTCCGCCTTCACTAC, R: TGCTTCTTTGAGAGTGATTGGA) Gas6 (F: CCGCGCCTACCAAGTCTTC, R: CGGGGTCGTTCTCGAACAC), Tgfb (F: GAGCCCGAAGCGGACTACTA, R: CACTGCTTCCCGAATGTCTGA), Il10 (F: GCCAGAGCCACATGCTCCTA, R: GTCCAGCTGGTCCTTTGTTTG), Nme1 (F: AGGAGACTTCTGCATCCAAGTT, R: TTCTGCGCACAGCTCTTG), Nme6 (F: TGATCAAGCCTGATGCAGTT, R: CGTTCGTACAATGAGGAACTTG); Suclg1 (F: CACATTCACAAGAAGGGAAGAAT, R: GGTTGTTTGGTGAACTGCTTC).

### Statistics

Data are expressed as mean+/- SEM. Statistical analysis was performed using a 2-tailed t test or ANOVA (with Tukey's post-test analysis) with GraphPad Prism software. A P value ≤ 0.05 was considered as statistically significant.

## Extended Data

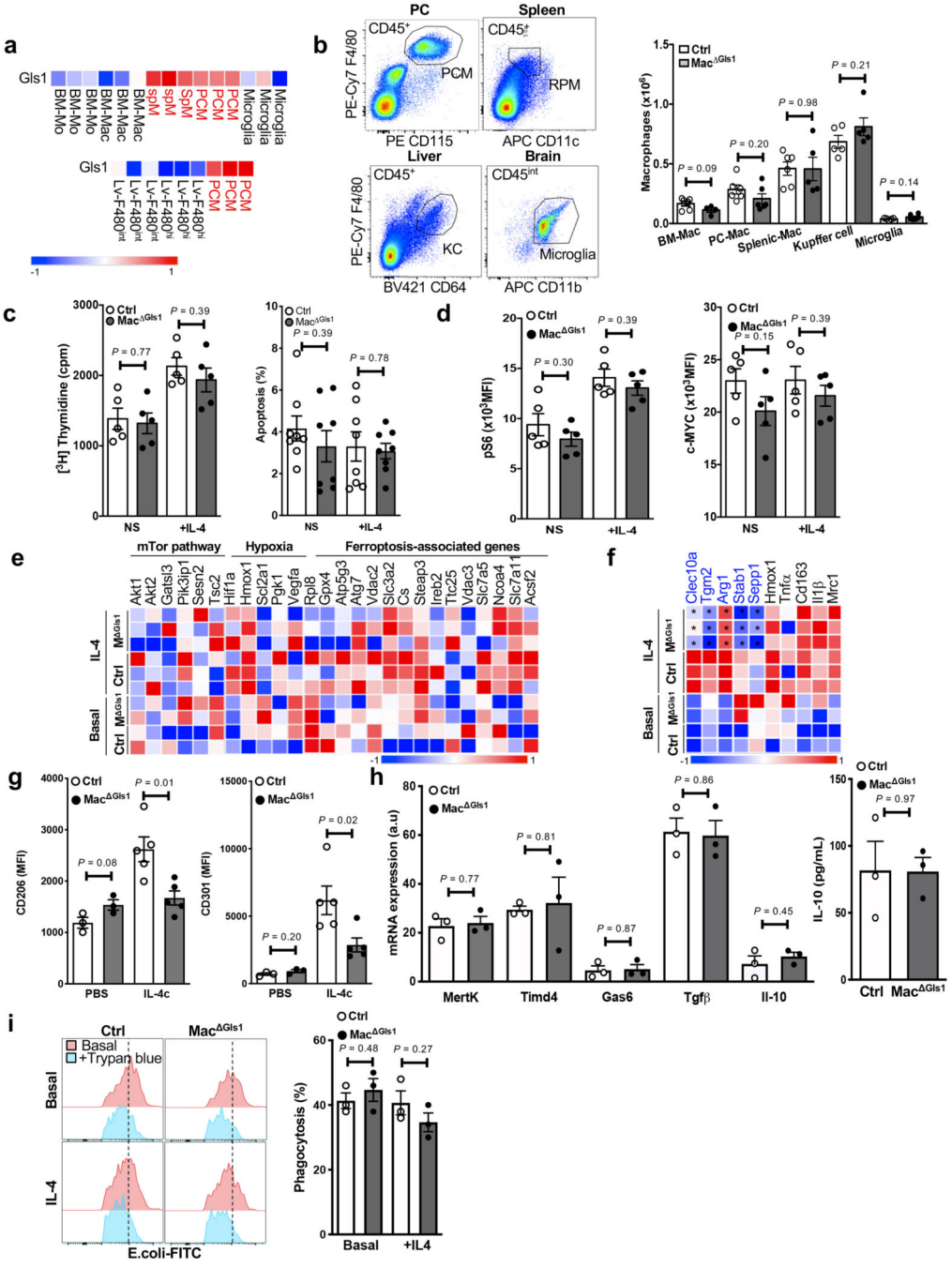


**Extended Data Fig. 1.**

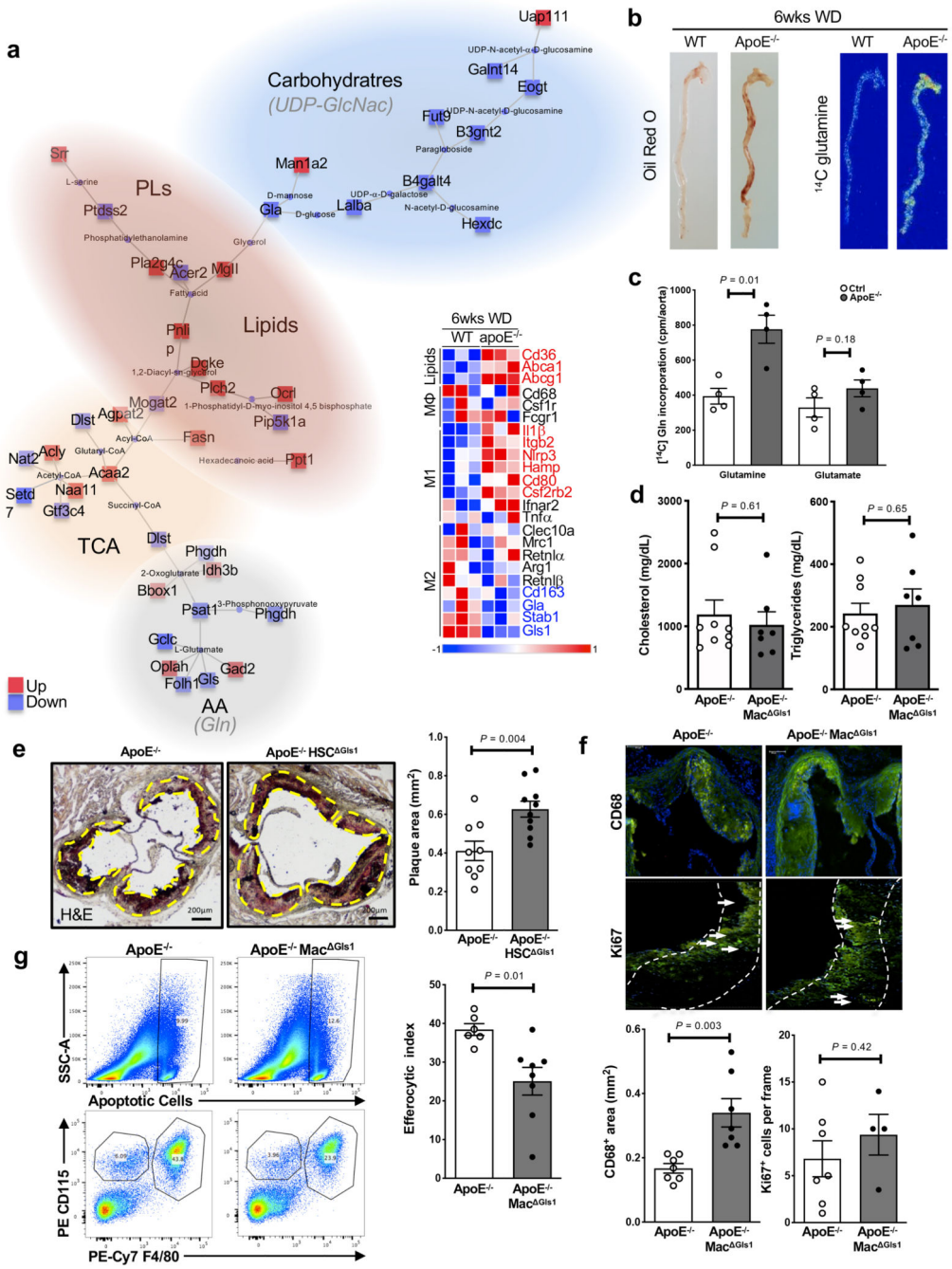


**Extended Data Fig. 2.**




Europe PMC Funders Author Manuscripts

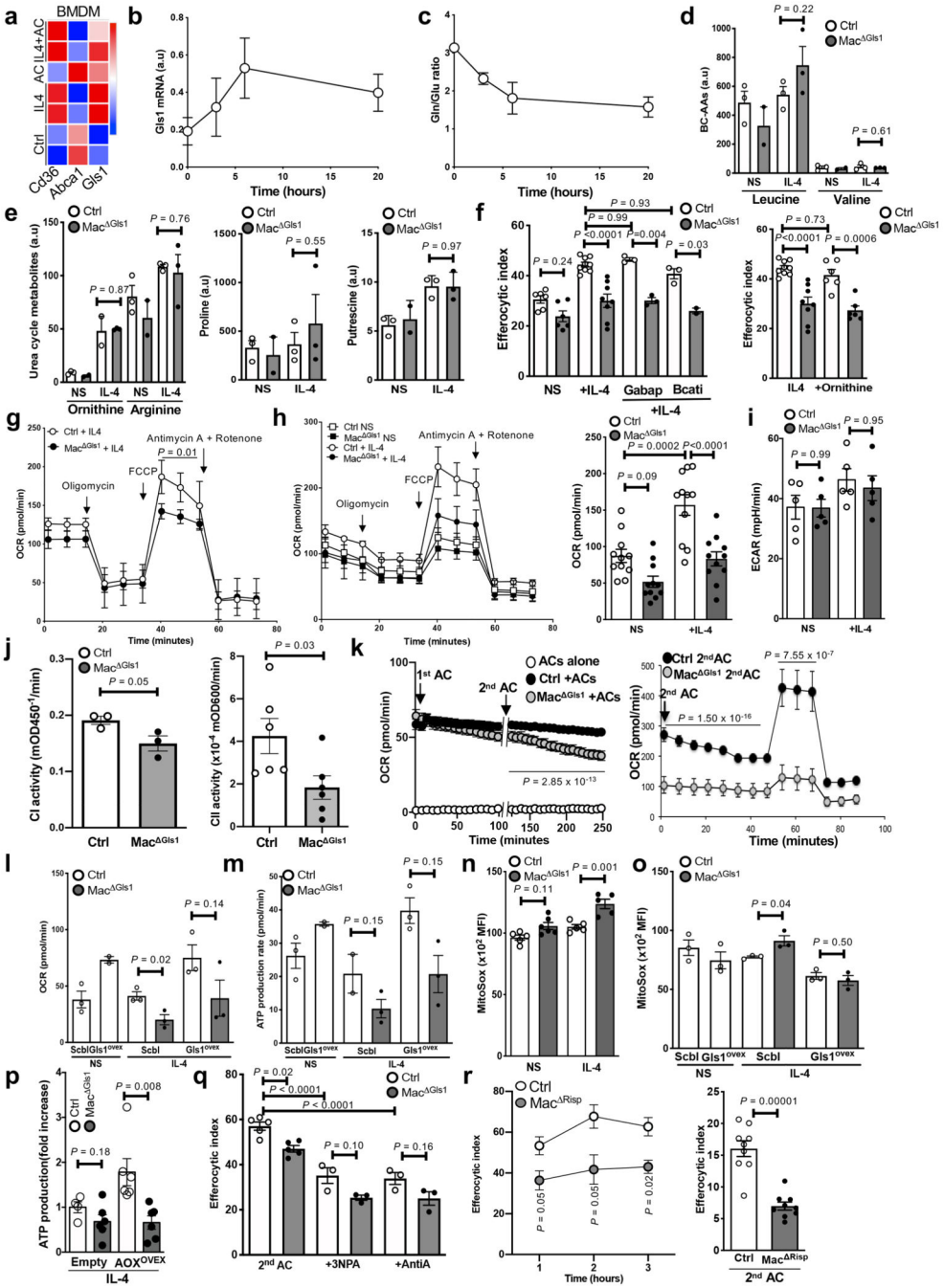

**Extended Data Fig. 3.**




Europe PMC Funders Author Manuscripts

Europe PMC Funders Author Manuscripts

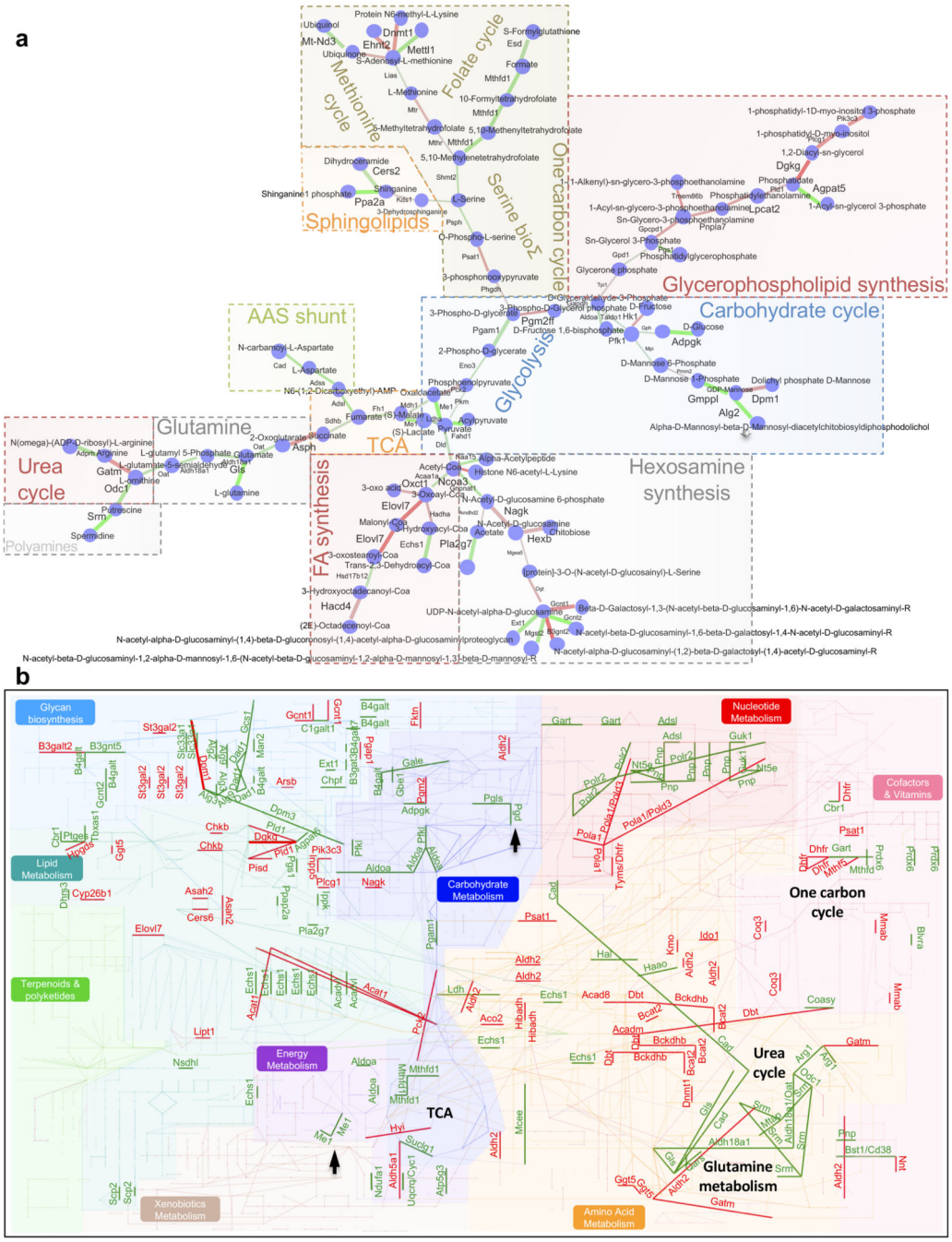


**Extended Data Fig. 4.**

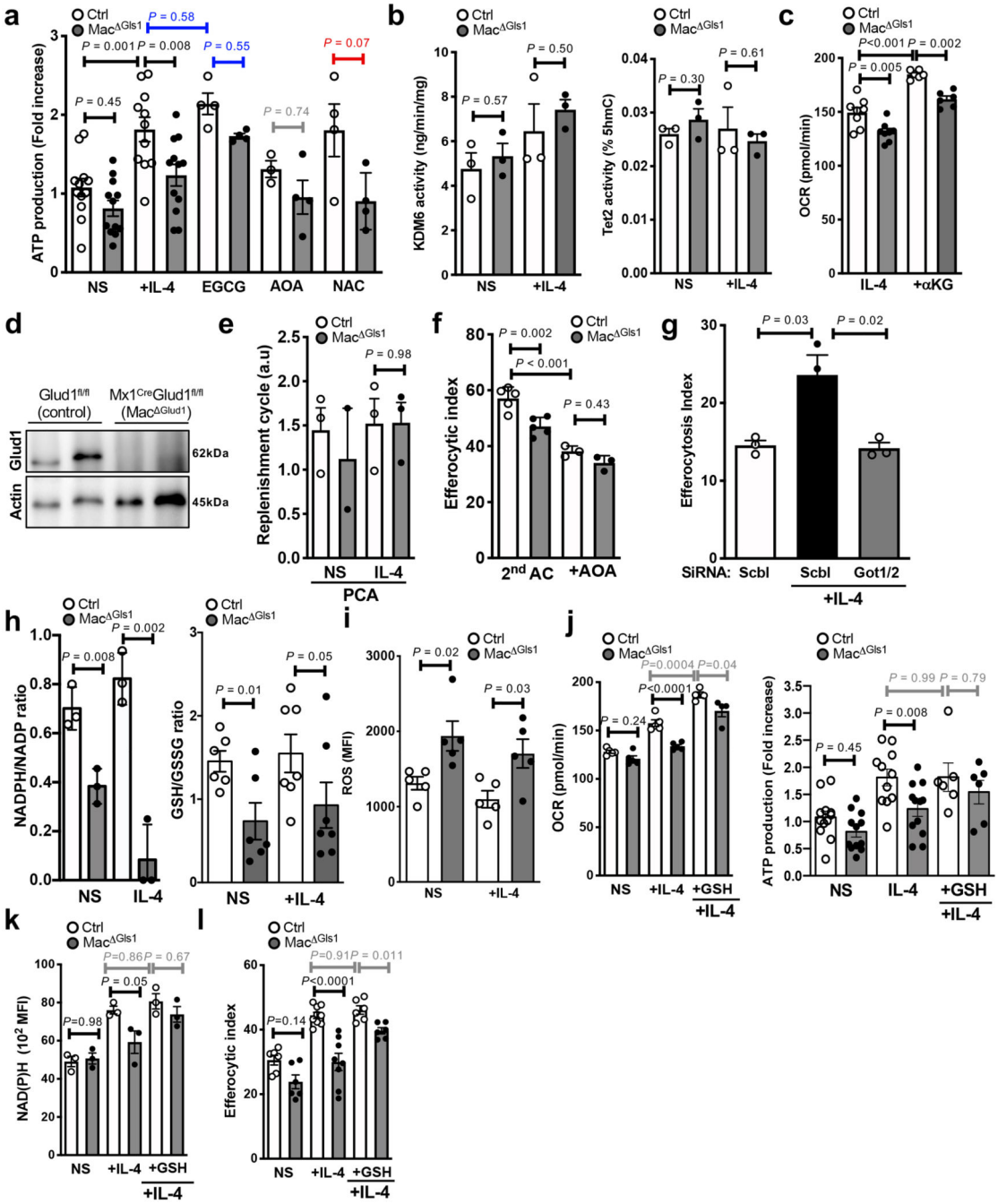


**Extended Data Fig. 5.**




Europe PMC Funders Author Manuscripts

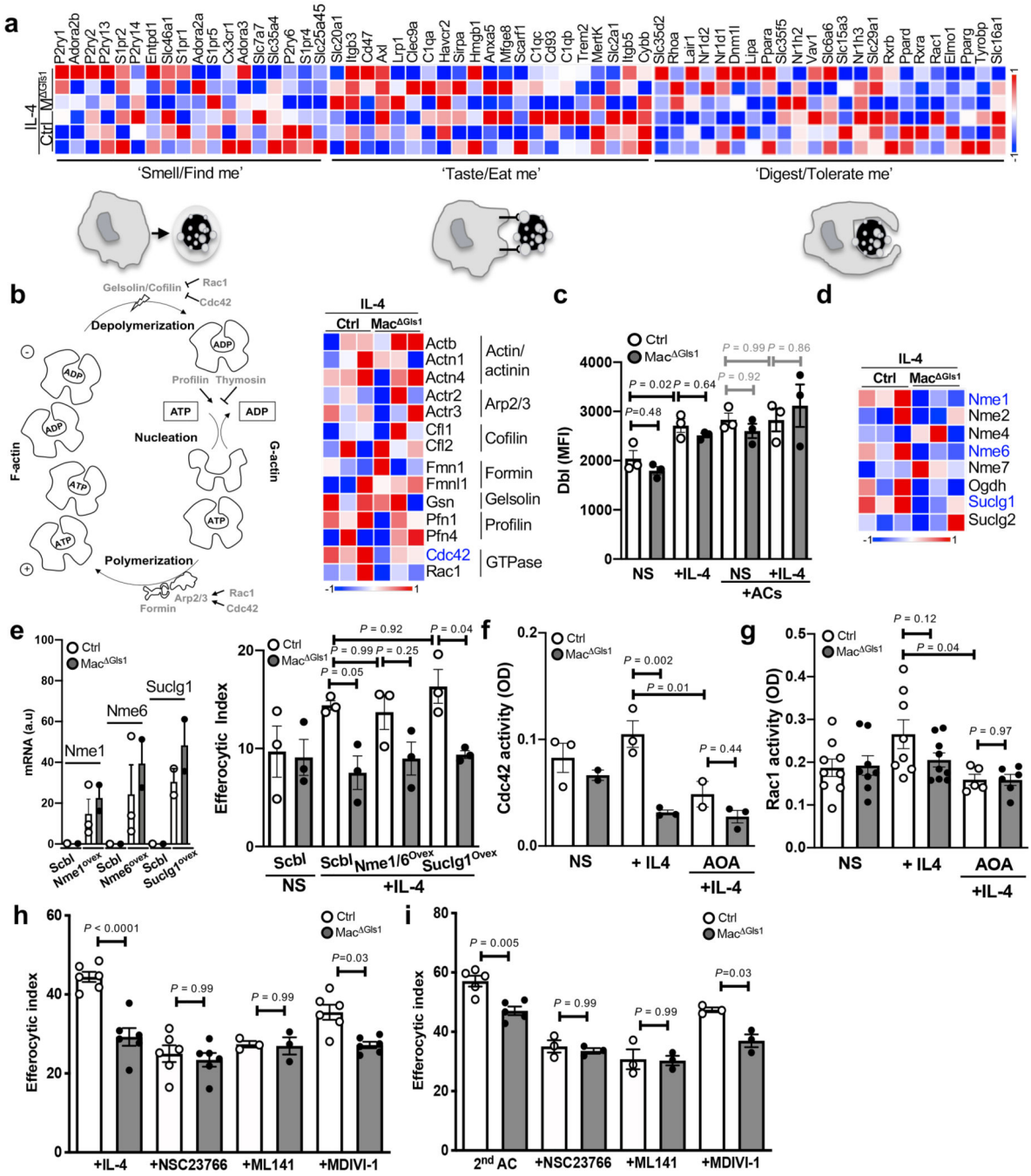


**Extended Data Fig. 6.**




Europe PMC Funders Author Manuscripts

Europe PMC Funders Author Manuscripts

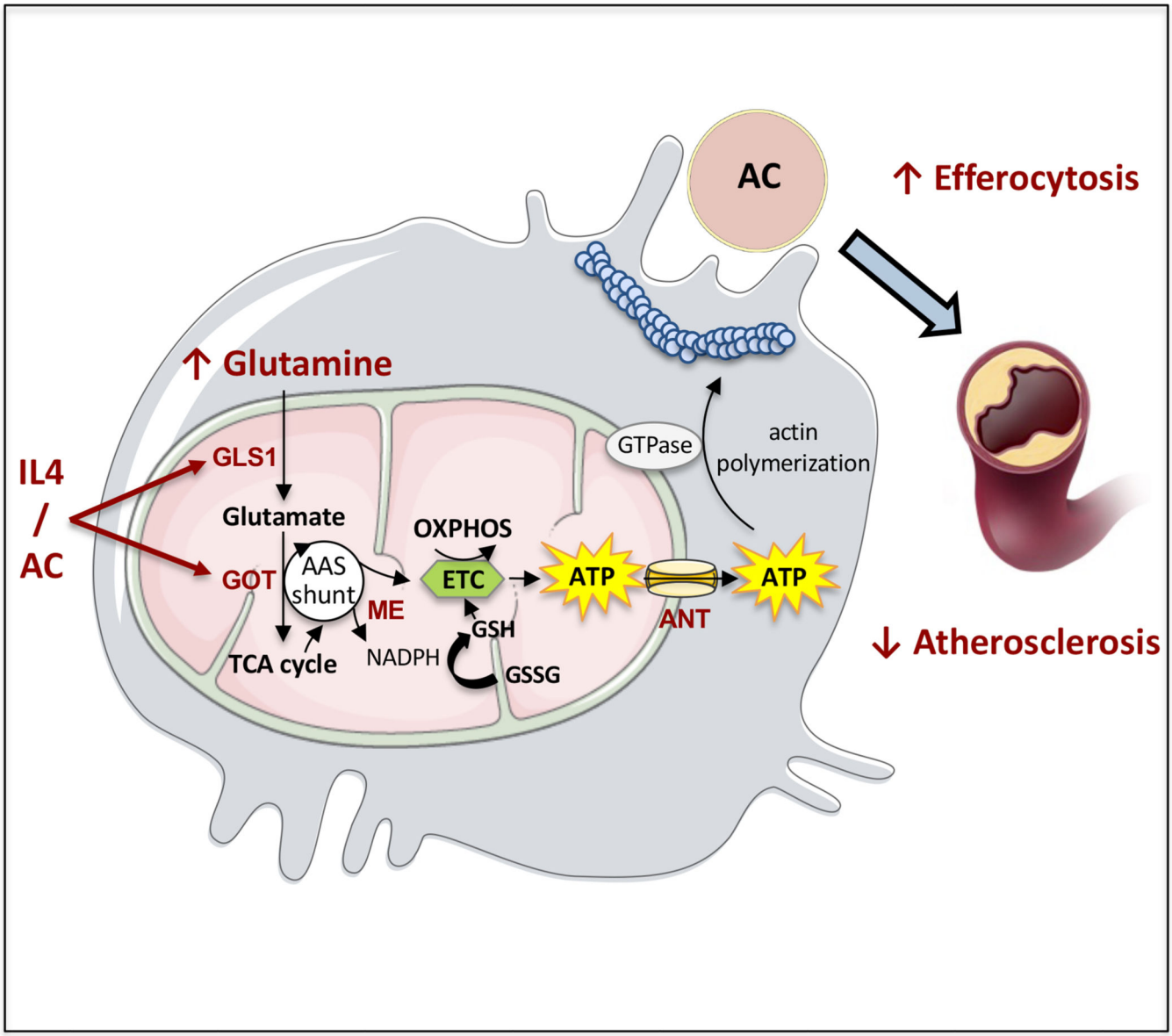


**Extended Data Fig. 7.**

## Supplementary Material

Refer to Web version on PubMed Central for supplementary material.

## Acknowledgments

We thank Béatrice Caraveo for computional development of DreamBio, a novel topological tool for Integrated Network Analysis. Nicolas Grandchamp provided Lenti-ONE AOX vector through Geg-tech. We thank Samantha Fernandez for the non-invasive study of atheroma plaques by ultrasound echography as part of the European Center for Research in Imaging (Cerimed), Dr Fréderic Labret for assistance with flow cytometry, Dr Véronique Corcelle for assistance in animal facilities and Dr. Marie Irondelle for assistance with confocal microscopy. This work was supported by grants from the Fondation de France (FDF) and the European Research Council (ERC) consolidator program (ERC2016COG724838) to L.Y.C. CCMA electron microscopy equipments have been funded by the Région Sud - Provence-Alpes-Côte d'Azur, the Conseil Départemental des Alpes Maritimes, and the GIS-IBiSA

Europe PMC Funders Author Manuscripts

## Data Availability

The data that support the findings of this study are available from the corresponding author upon reasonable request. Topological analyses are available at artyomovlab.wustl.edu/shiny/gam and at biotest.hematometabolism.science upon request. Raw and processed sequencing are deposited to PubMed GEO under GSE183176.

## References


1. Kojima Y, Weissman IL, Leeper NJ. The Role of Efferocytosis in Atherosclerosis. Circulation. 2017; 135 :476–489. [PubMed: 28137963]
2. Elliott MR, Ravichandran KS. The Dynamics of Apoptotic Cell Clearance. Dev Cell. 2016; 38 :147–160. [PubMed: 27459067]
3. Wang Y, et al. Mitochondrial Fission Promotes the Continued Clearance of Apoptotic Cells by Macrophages. Cell. 2017; 171 :331–345. e22 [PubMed: 28942921]
4. Yurdagul A Jr, et al. Macrophage Metabolism of Apoptotic Cell-Derived Arginine Promotes Continual Efferocytosis and Resolution of Injury. Cell Metab. 2020; 31 :518–533. e10 [PubMed: 32004476]
5. Bosurgi L, et al. Macrophage function in tissue repair and remodeling requires IL-4 or IL-13 with apoptotic cells. Science. 2017; 356 :1072–1076. [PubMed: 28495875]
6. Han CZ, Ravichandran KS. Metabolic connections during apoptotic cell engulfment. Cell. 2011; 147 :1442–1445. [PubMed: 22196723]
7. DeBerardinis RJ, Cheng T. Q's next: the diverse functions of glutamine in metabolism, cell biology and cancer. Oncogene. 2010; 29 :313–324. [PubMed: 19881548]
8. O'Neill LA, Pearce EJ. Immunometabolism governs dendritic cell and macrophage function. J Exp Med. 2016; 213 :15–23. [PubMed: 26694970]
9. Jha AK, et al. Network integration of parallel metabolic and transcriptional data reveals metabolic modules that regulate macrophage polarization. Immunity. 2015; 42 :419–430. [PubMed: 25786174]
10. Morioka S, et al. Efferocytosis induces a novel SLC program to promote glucose uptake and lactate release. Nature. 2018; 563 :714–718. [PubMed: 30464343]
11. Zhang S, et al. Efferocytosis Fuels Requirements of Fatty Acid Oxidation and the Electron Transport Chain to Polarize Macrophages for Tissue Repair. Cell Metab. 2019; 29 :443–456. e445 [PubMed: 30595481]
12. Dixon SJ, et al. Ferroptosis: an iron-dependent form of nonapoptotic cell death. Cell. 2012; 149 :1060–1072. [PubMed: 22632970]
13. Nicklin P, et al. Bidirectional transport of amino acids regulates mTOR and autophagy. Cell. 2009; 136 :521–534. [PubMed: 19203585]
14. Tabas I. Macrophage death and defective inflammation resolution in atherosclerosis. Nat Rev Immunol. 2010; 10 :36–46. [PubMed: 19960040]
15. Grabner R, et al. Lymphotoxin beta receptor signaling promotes tertiary lymphoid organogenesis in the aorta adventitia of aged ApoE-/-mice. J Exp Med. 2009; 206 :233–248. [PubMed: 19139167]
16. Jais A, et al. Heme oxygenase-1 drives metaflammation and insulin resistance in mouse and man. Cell. 2014; 158 :25–40. [PubMed: 24995976]
17. Vats D, et al. Oxidative metabolism and PGC-1beta attenuate macrophage-mediated inflammation. Cell Metab. 2006; 4 :13–24. [PubMed: 16814729]
18. Perales-Clemente E, et al. Restoration of electron transport without proton pumping in mammalian mitochondria. Proc Natl Acad Sci U S A. 2008; 105 :18735–9. [PubMed: 19020091]
19. Fernandez-Ayala DJ, et al. Expression of the Ciona intestinalis alternative oxidase (AOX) in Drosophila complements defects in mitochondrial oxidative phosphorylation. Cell Metab. 2009; 9 :449–60. [PubMed: 19416715]

20. Chandel NS. Evolution of Mitochondria as Signaling Organelles. Cell Metab. 2015; 22 :204–206. [PubMed: 26073494]
21. Caron E, Hall A. Identification of two distinct mechanisms of phagocytosis controlled by different Rho GTPases. Science. 1998; 282 :1717–21. [PubMed: 9831565]
22. A-Gonzalez N, et al. Apoptotic cells promote their own clearance and immune tolerance through activation of the nuclear receptor LXR. Immunity. 2009; 31 :245–58. [PubMed: 19646905]
23. Yvan-Charvet L, et al. ABCA1 and ABCG1 protect against oxidative stress-induced macrophage apoptosis during efferocytosis. Circ Res. 2010; 106 :1861–1869. [PubMed: 20431058]
24. Viaud M, et al. Lysosomal Cholesterol Hydrolysis Couples Efferocytosis to Anti-Inflammatory Oxysterol Production. Circ Res. 2018; 122 :1369–1384. [PubMed: 29523554]
25. Tavakoli S, et al. Characterization of Macrophage Polarization States Using Combined Measurement of 2-Deoxyglucose and Glutamine Accumulation: Implications for Imaging of Atherosclerosis. Arterioscler Thromb Vasc Biol. 2017; 37 :1840–1848. [PubMed: 28798141]
26. Johnson MO, et al. Distinct Regulation of Th17 and Th1 Cell Differentiation by Glutaminase-Dependent Metabolism. Cell. 2018; 175 :1780–1795. e19 [PubMed: 30392958]
27. Papathanassiu AE, et al. BCAT1 controls metabolic reprogramming in activated human macrophages and is associated with inflammatory diseases. Nat Commun. 2017; 8 16040 [PubMed: 28699638]
28. O'Neill LA, Artyomov MN. Itaconate: the poster child of metabolic reprogramming in macrophage function. Nat Rev Immunol. 2019; 19 :273–281. [PubMed: 30705422]
29. Liu PS, et al. alpha-ketoglutarate orchestrates macrophage activation through metabolic and epigenetic reprogramming. Nat Immunol. 2017; 18 :985–994. [PubMed: 28714978]
30. Scialò F, Fernández-Ayala DJ, Sanz A. Role of Mitochondrial Reverse Electron Transport in ROS Signaling: Potential Roles in Health and Disease. Front Physiol. 2017; 8 :428. [PubMed: 28701960]
31. Murphy MP. How mitochondria produce reactive oxygen species. Biochem J. 2009; 417 :1–13. [PubMed: 19061483]
32. Lapuente-Brun E, et al. Supercomplex assembly determines electron flux in the mitochondrial electron transport chain. Science. 2013; 340 :1567–70. [PubMed: 23812712]
33. Guarás A, et al. The CoQH2/CoQ Ratio Serves as a Sensor of Respiratory Chain Efficiency. Cell Rep. 2016; 15 :197–209. [PubMed: 27052170]
34. Stipanuk MH, Caudill MA. Biochemical, physiological and molecular aspects of human nutrition. 2013
35. Jin H, et al. Integrative multiomics analysis of human atherosclerosis reveals a serum response factor-driven network associated with intraplaque hemorrhage. Clin Transl Med. 2021; 11 e458 [PubMed: 34185408]
36. Gautier EL, et al. Gene-expression profiles and transcriptional regulatory pathways that underlie the identity and diversity of mouse tissue macrophages. Nat Immunol. 2012; 13 :1118–1128. [PubMed: 23023392]
37. Devos M, et al. Keratinocyte Expression of A20/TNFAIP3 Controls Skin Inflammation Associated with Atopic Dermatitis and Psoriasis. J Invest Dermatol. 2019; 139 :135–145. [PubMed: 30118730]
38. Aidoud N, et al. A combination of lipidomics, MS imaging, and PET scan imaging reveals differences in cerebral activity in rat pups according to the lipid quality of infant formulas. FASEB J. 2018; 32 :4776–4790. [PubMed: 29565735]

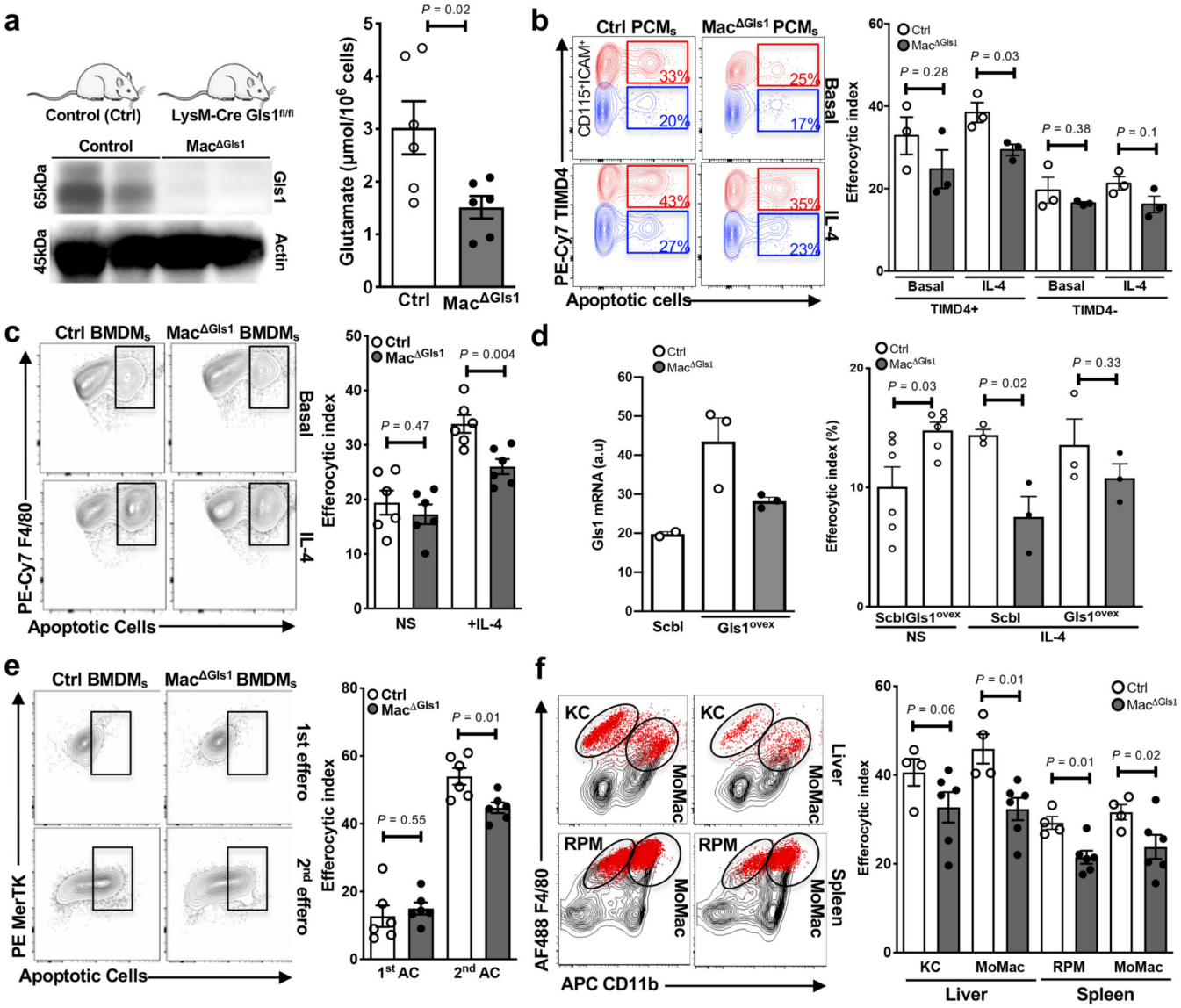


**Figure 1. Macrophage-*Gls1* deletion impairs efferocytosis *in vitro* and *in vivo*.**

**(a)** Western blot of GLS1 protein (left) and glutamate levels (right) in *Gls1* $^{fl/fl}$ control and Mac$^{\Delta Gls1}$ PCMs. **(b)** Efferocytic index gating strategy (left) and quantification (right) measured by flow cytometry after 45min exposure with apoptotic cells (ACs) in *Cre*$^{+}$ control and Mac$^{\Delta Gls1}$ PCMs at steady state (resting condition) or after overnight IL-4 stimulation (reparative condition). **(c)** Similar experiments were performed in resting and reparative control (both *Gls1* $^{fl/fl}$ and *Cre*$^{+}$) and Mac$^{\Delta Gls1}$ BMDMs. Efferocytic index was calculated as follows: (number of macrophages with ACs/total number of macrophages) × 100. **(d)** qPCR quantification (left) and efferocytic index (right) in *Gls1* $^{fl/fl}$ control and Mac$^{\Delta Gls1}$ BMDMs stimulated overnight with IL-4 after *Gls1* lentivirus overexpression. **(e)** Efferocytic index gating strategy (left) and quantification (right) measured by flow cytometry after one (45min) or two (45min + 1-hour rest + 45min) incubations with ACs (resolving condition) in control (both *Gls1* $^{fl/fl}$ and *Cre*$^{+}$) and Mac$^{\Delta Gls1}$ BMDMs. **(f)** Efferocytic index gating

strategy (left) and quantification (right) measured by flow cytometry in *Gls1* $^{fl/fl}$ control and Mac$^{\Delta Gls1}$ Kupffer cells (KC), red pulp macrophages (RPM) and monocyte-derived macrophages (MoMac) after labelled apoptotic thymocytes *i.v.* injection. Both sexes were analyzed. All values are mean ± SEM and are representative of at least one independent experiment ($n$=6 independent animals for **a, c, e**, $n$=3 to 6 for **d**, $n$=3 for **b**). Western blot results in **a** are representative experiments of two biologically independent replicates. *P* values were determined by two-tailed Student's t-test. Source data are provided as a Source Data file (**a-f**).



Europe PMC Funders Author Manuscripts

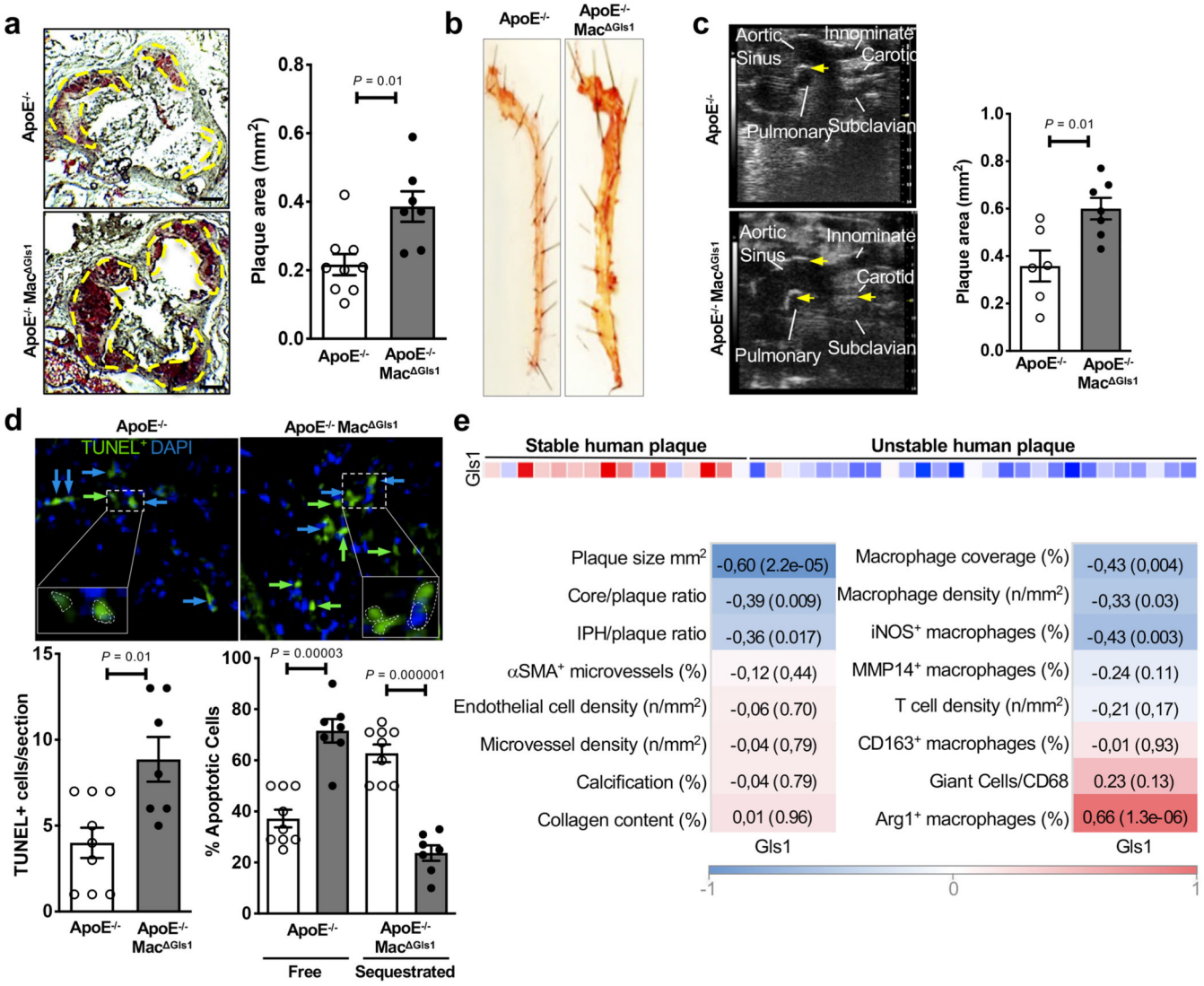


**Figure 2. Myeloid-*Gls1* deletion impairs efferocytosis in the pathological process of atherosclerosis.**

**(a)** Representative sections (left) and quantification (right) of aortic plaques from *Apoe*$^{-/-}$ or *Apoe*$^{-/-}$ Mac$^{\Delta Gls1}$ mice (12 weeks WD) stained for Oil Red O and Hematoxylin Eosin. Scale bar: 200μm. Both sexes were analyzed. **(b)** Oil red O stained descending aortas from representative female *Apoe*$^{-/-}$ or *Apoe*$^{-/-}$ Mac$^{\Delta Gls1}$ mice maintained on a WD for 12 weeks. **(c)** Echography (left) and quantification (right) of aortic plaques from male *Apoe*$^{-/-}$ or *Apoe*$^{-/-}$ Mac$^{\Delta Gls1}$ mice fed for 12 weeks on WD. Arrows indicate plaque areas. **(d)** Representative images (top) and quantification (bottom) of TUNEL$^{+}$ cells (green) in aortic plaques from *Apoe* $^{-/-}$ or *Apoe*$^{-/-}$ Mac$^{\Delta Gls1}$ mice (12 weeks WD). Sections were counterstained with DAPI (blue). TUNEL positive apoptotic cell (AC) either free (TUNEL-positive considered as apoptotic bodies) or cell sequestrated (TUNEL-positive associated with large cellular nuclei considered as efferocytes) was quantified. All values are mean ± SEM and are representative of at least one independent experiment ($n$=6 to 9 independent animals for **a, c, d**). *P* values were determined by two-tailed Student's t-test. Source data




Europe PMC Funders Author Manuscripts

are provided as a Source Data file (**a, c, d**). **(e)** Correlation between Gls1 expression and human atherosclerotic plaque complexity in the Maastricht Pathology collection (Results are from 16 stable segments and 27 unstable segments; red indicates positive and blue negative correlations).



Europe PMC Funders Author Manuscripts

Europe PMC Funders Author Manuscripts

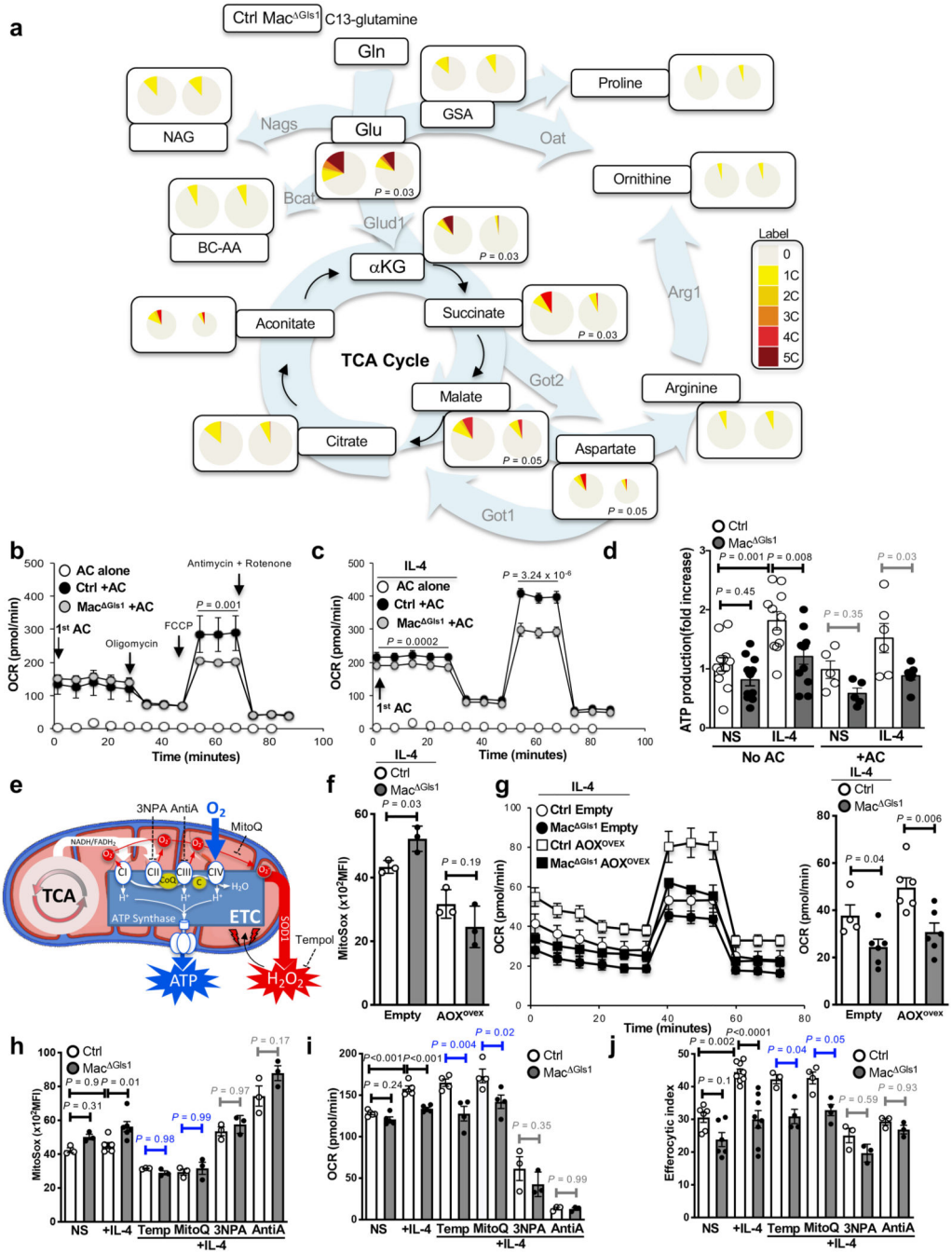


**Figure 3. Glutamine metabolism fuels mitochondrial oxidative phosphorylation (OXPHOS) to support efferocytosis.**

**(a)** Carbon fluxes using U-13C-glutamine. U-13C glutamine was added in the medium of reparative IL-4 treated macrophages for 4 hours. Circle sizes are scaled with respect to pool size for individual metabolites and the number of carbon incorporated from U-13C glutamine is indicated by color code. Thin black arrows represent known metabolic pathway connections; background arrows indicate deduced major metabolic flows in reparative macrophages. Grey to dark red indicate increased number of carbons. **(b)** OCR

measured by Seahorse after one incubation with ACs in control or Mac$^{\Delta Gls1}$ BMDMs in resting conditions or **(c)** stimulated overnight with IL-4. **(d)** ATP production measured by Seahorse in resting and reparative control or Mac$^{\Delta Gls1}$ BMDMs after one or no round of efferocytosis. **(e)** Schematic representation of mitochondria electron transport chain and its pharmacological inhibitors. **(f)** Mitochondrial ROS quantification using MitoSox by flow cytometry in reparative control or Mac$^{\Delta Gls1}$ BMDMs after lentiviral vector-mediated overexpression of mitochondrial alternative oxidase (AOX) from *Ciona intestinalis*. **(g)** OCR measured by Seahorse in these cells. **(h)** MitoSox quantification, **(i)** OCR quantification and **(j)** efferocytic index in control or Mac$^{\Delta Gls1}$ BMDMs at steady state or after overnight IL-4 stimulation +/- Tempol, Mitoquinol, 3NPA or antimicyn A. All values are mean ± SEM and are representative of at least one experiment ($n$=6 for **a**, $n$= 5 to 12 for **b-d**, $n$=3 for **f-h**, $n$=3 to 9 for **i,j** of biologically independent replicates). $P$ values were determined by ordinary two-tailed Student's t-test (**a, b, c, f, g**) or one-way ANOVA with Tukey post hoc test for multiple comparisons (**d, h, i, j**). Each statistical bar color-coded represents an independent one-way ANOVA test. Source data are provided as a Source Data table (**a**) or Source Data file (**b-d, f-j**).



Europe PMC Funders Author Manuscripts

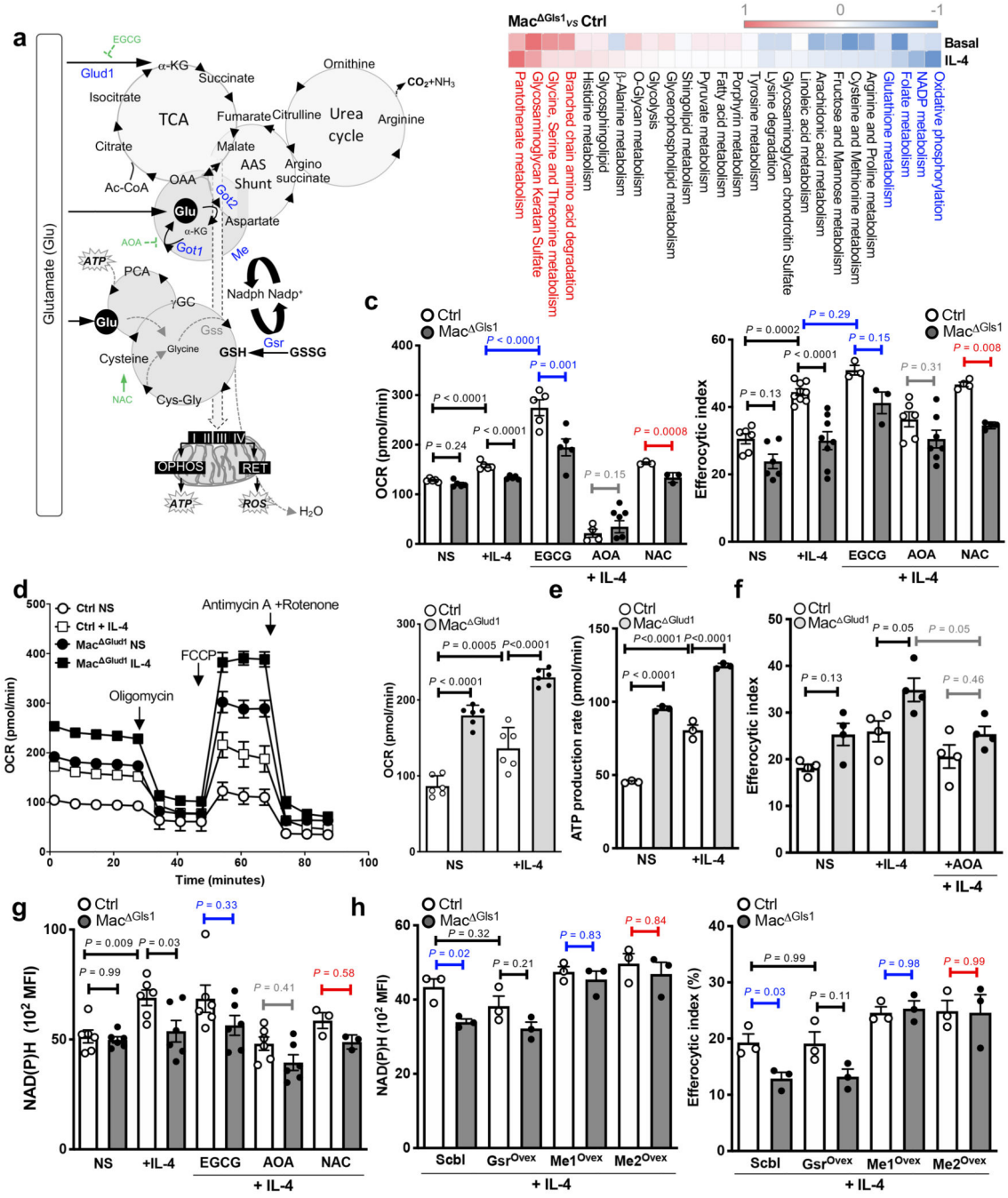


**Figure 4. Non-canonical transaminase pathway allows glutaminolysis to fuel OXPHOS and support efferocytosis.**

**(a)** Schematic representation of glutamate incorporation into metabolic cycles. Red indicates up- and blue down-regulated pathways **(b)** Pathway enrichment analysis of RNA-seq profiling in resting and reparative control or Mac$^{\Delta Gls1}$ PCMs. Pathways highlighted in red and blue indicated significant up- or down-regulation, respectively. **(c)** OCR quantification (left panel) and efferocytic index (right panel) in control or Mac$^{\Delta Gls1}$ BMDMs at steady state or after overnight IL-4 stimulation +/- EGCG, AOA or NAC. **(d)** OCR measurements




Europe PMC Funders Author Manuscripts

and **(e)** ATP production rate measured by Seahorse and **(f)** efferocytic index in control or $Mac^{\Delta Glud1}$ BMDMs at steady state or after overnight IL-4 stimulation +/- AOA. **(g)** NAD(P)H levels as assessed by endogenous fluorescence in control or $Mac^{\Delta Gls1}$ BMDMs at steady state or after overnight IL-4 stimulation +/- EGCG, AOA or NAC. **(h)** NAD(P)H levels (left panel) and efferocytic index (right panel) in reparative control or $Mac^{\Delta Gls1}$ BMDMs after lentiviral vector-mediated overexpression of empty, glutathione-disulfide reductase (*Gsr*) or malic enzymes (*Me1* and *Me2*). All values are mean ± SEM and are representative of at least one experiment ($n$=5 for **c** (*left*), $n$= 3 to 12 for **c** (*right*), $n$=6 for **d**, $n$=3 for **e,h**, $n$=4 for **f**, $n$=6 for **g** of biologically independent replicates). $P$ values were determined by ordinary one-way ANOVA with Tukey post hoc test for multiple comparisons (**c-h**). Each statistical bar color-coded represents an independent one-way ANOVA test against IL-4 conditions. Source data are provided as a Source Data file (**c-h**).

Europe PMC Funders Author Manuscripts

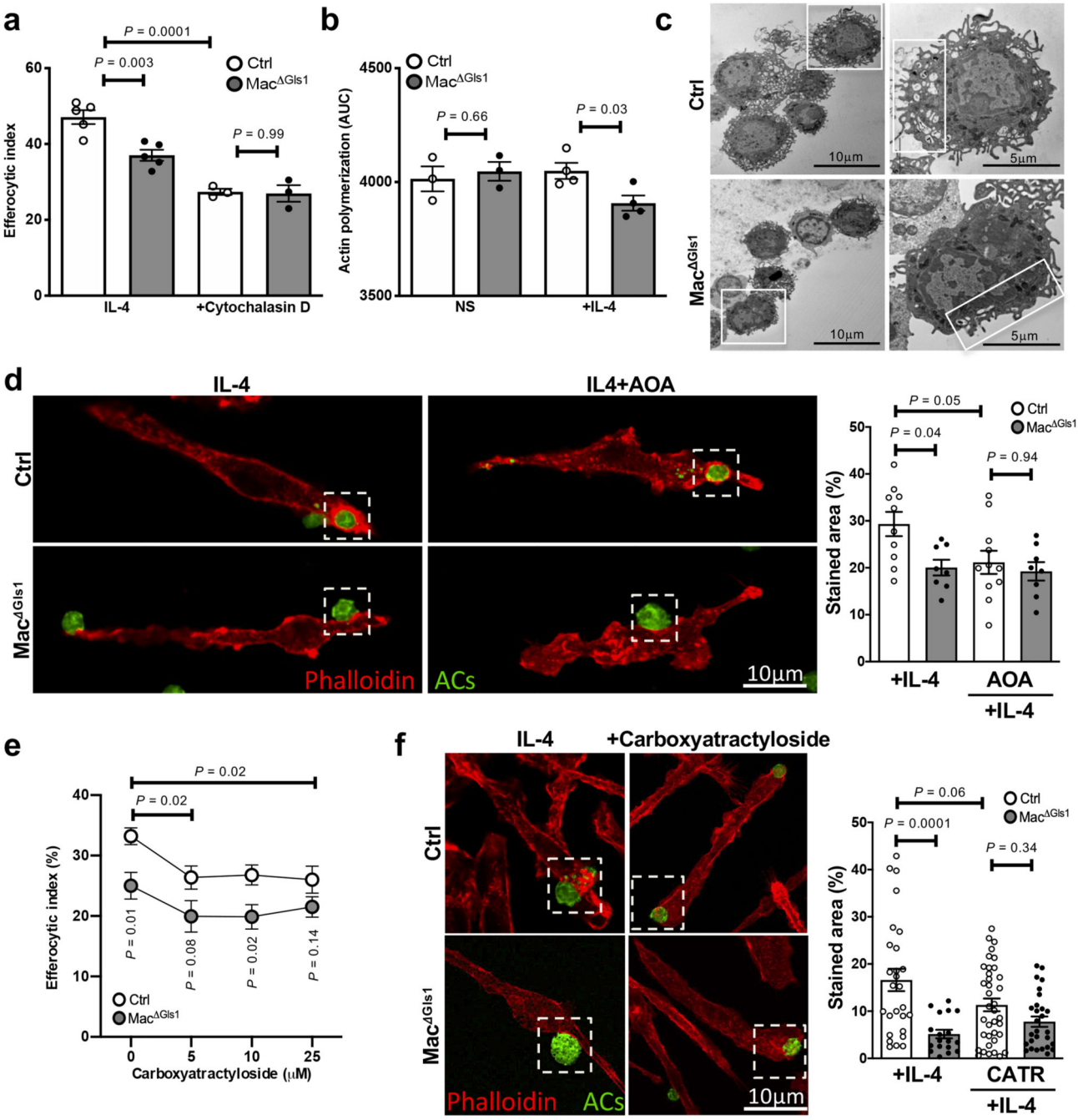


**Figure 5. Glutamine metabolism supports the high-energy requirement of cytoskeletal rearrangement and corpse engulfment.**

**(a)** Quantification of AC binding and internalization after treatment with 5µM cytochalasin D for 15 min before the addition of AC in control or Mac$^{\Delta Gls1}$ BMDMs stimulated overnight +/- IL-4. **(b)** Actin polymerization assay in resting and reparative control or Mac$^{\Delta Gls1}$ BMDMs. **(c)** Transmission electron microscopy imaging of control or Mac$^{\Delta Gls1}$ PCMs. Left scale bar: 10µm. Right scale bar: 5µm. **(d)** Representative images of control or Mac$^{\Delta Gls1}$ BMDMs stimulated overnight with IL-4 in presence or absence of AOA and stained for

F-actin (Red) and ACs (green). Scale bar: 10μm. F-actin staining localized around the phagocytic cup was quantified. **(e)** Efferocytic index in reparative control or $Mac^{\Delta Gls1}$ BMDMs after treatment with the indicated concentrations of carboxyatractyloside (CATR) for 15 min before the addition of AC. **(f)** Representative images and quantification of F-actin staining localized around the phagocytic cup after treatment with 5μM CATR for 15 min before the addition of AC. All values are mean ± SEM and are representative of at least one experiment ($n$=3-5 for **a**, $n$=3 for **b,e** of biologically independent replicates; $n$=9-11 for **d**, $n$=18-39 for **f** of biologically independent measurements). $P$ values were determined by ordinary two-tailed Student's t-test (**b, e**) or one-way ANOVA with Tukey post hoc test for multiple comparisons (**a, d, f**). Source data are provided as a Source Data file (**a-b, d-f**).



Europe PMC Funders Author Manuscripts